









# Preparation of $\text{SrMg}_x\text{Ru}_{1-x}\text{O}_3$ Thin Films by Pulsed Laser Deposition

by

Mohammad Mehdi Yazdanian

A THESIS SUBMITTED IN PARTIAL FULFILMENT OF  
THE REQUIREMENTS FOR THE DEGREE OF

MASTER OF SCIENCE

in

The Faculty of Mathematics and Sciences

Department of Physics

BROCK UNIVERSITY

May 28, 2004

2003 © Mohammad Mehdi Yazdanian



In presenting this thesis in partial fulfilment of the requirements for an advanced degree at the Brock University, I agree that the Library shall make it freely available for reference and study. I further agree that permission for extensive copying of this thesis for scholarly purposes may be granted by the head of my department or by his or her representatives. It is understood that copying or publication of this thesis for financial gain shall not be allowed without my written permission.

(Signature) \_\_\_\_\_

Department of Physics

Brock University  
St.Catharines, Canada

Date \_\_\_\_\_



# Abstract

$\text{SrMg}_x\text{Ru}_{1-x}\text{O}_3$  thin films were made by using pulsed laser deposition on  $\text{SrTiO}_3$  (100) substrates in either  $\text{O}_2$  or Ar atmosphere. The thin films were characterized by x-ray diffraction, energy dispersive x-ray microanalysis, dc resistivity measurement, and dc magnetization measurement. The effect of Mg doping was observed. As soon as the amount of Mg increased in  $\text{SrMg}_x\text{Ru}_{1-x}\text{O}_3$  thin films, the magnetization decreased, and the resistivity increased. It had little effect on the Curie temperature (transition temperature). The magnetization states of  $\text{SrMg}_x\text{Ru}_{1-x}\text{O}_3$  thin films, for  $x < 0.15$ , are similar to  $\text{SrRuO}_3$  films. X-ray diffraction results for  $\text{SrMg}_x\text{Ru}_{1-x}\text{O}_3$  thin films made in oxygen showed that the films are epitaxial. The thin films could not be well made in Ar atmosphere during laser ablation as there was no clear peak of  $\text{SrMg}_x\text{Ru}_{1-x}\text{O}_3$  in x-ray diffraction results. Substrate temperatures had an effect on the resistivity of the films. The residual resistivity ratios were increased by increasing substrate temperature. It was observed that the thickness of thin films are another factor for film quality: Thin films were epitaxial, but thicker films were not epitaxial.



# Contents

Abstract . . . . .	ii
Contents . . . . .	iii
List of Tables . . . . .	vi
List of Figures . . . . .	vii
Acknowledgements . . . . .	xi
1 Introduction . . . . .	1
2 Ablation Targets and Thin Films . . . . .	6
2.1 Instruction for making polycrystalline $\text{SrMg}_x\text{Ru}_{1-x}\text{O}_3$ . . . . .	6
2.2 X-ray Diffraction-Guinier Camera . . . . .	7
2.2.1 X-ray data for ablation targets . . . . .	8
2.3 Pulsed laser deposition . . . . .	13
2.3.1 Thin film-Laser ablation method . . . . .	14
2.4 X-ray data for thin films . . . . .	16
2.4.1 $\text{SrRuO}_3$ thin film-DM9 . . . . .	18



---

2.4.2	$\text{SrMg}_{0.05}\text{Ru}_{0.95}\text{O}_3$ thin film-DM20/22 . . . . .	18
2.4.3	$\text{SrMg}_{0.1}\text{Ru}_{0.9}\text{O}_3$ thin film-DM16 and DM19/24 . . . . .	21
2.4.4	$\text{SrMg}_{0.15}\text{Ru}_{0.85}\text{O}_3$ thin film-DM13/15/25 . . . . .	24
2.5	Lattice parameters of thin films . . . . .	24
<b>3</b>	<b>Magnetization . . . . .</b>	<b>35</b>
3.1	Magnetism in metals and insulators . . . . .	35
3.1.1	Paramagnetism and Ferromagnetism . . . . .	35
3.1.2	The Curie-Weiss Model . . . . .	36
3.1.3	Ferromagnetism in Insulators . . . . .	37
3.1.4	Ferromagnetism in metals - itinerant model . . . . .	38
3.2	Procedure and discussion . . . . .	39
3.2.1	Magnetic properties of polycrystalline $\text{SrMg}_x\text{Ru}_{1-x}\text{O}_3$ . . . . .	39
3.2.2	Magnetic properties of $\text{SrTiO}_3$ substrate . . . . .	40
3.2.3	Magnetic properties of $\text{SrMg}_x\text{Ru}_{1-x}\text{O}_3$ thin films . . . . .	41
<b>4</b>	<b>Resistivity . . . . .</b>	<b>55</b>
4.1	Theory of resistivity in metals and insulators . . . . .	55
4.1.1	Resistivity in metals . . . . .	55
4.1.2	Resistivity in insulators . . . . .	56
4.1.3	Variable-range hopping . . . . .	60
4.2	Preparing Thin Films for Measurement . . . . .	63
4.3	Result and Graphs . . . . .	65
4.3.1	Resistivity of $\text{SrRuO}_3$ thin films . . . . .	65



---

4.3.2	Resistivity of $\text{SrMg}_x\text{Ru}_{1-x}\text{O}_3$ thin films . . . . .	66
4.3.3	Low temperature resistivity in insulating samples . . .	67
5	Conclusions . . . . .	80
	Bibliography . . . . .	82



# List of Tables

1.1	Thinfilms, a summary of previous work . . . . .	2
2.1	Experimental raw material mass ratios for making $\text{SrMg}_x\text{Ru}_{1-x}\text{O}_3$	7
2.2	Distances of the negatives for ZnS . . . . .	9
2.3	1.d spacing for polycrystalline $\text{SrMg}_x\text{Ru}_{1-x}\text{O}_3$ targets . . . . .	11
2.4	2.d spacing for polycrystalline $\text{SrMg}_x\text{Ru}_{1-x}\text{O}_3$ targets . . . . .	12
2.5	Thin film growth parameters . . . . .	17
2.6	Lattice parameters of SRO thin films on a STO substrate . . .	34
3.1	Number of $\mu_B$ per Ru atom for polycrystalline $\text{SrMg}_x\text{Ru}_{1-x}\text{O}_3$ in paramagnetic state . . . . .	42
4.1	$\text{SrMg}_x\text{Ru}_{1-x}\text{O}_3$ Film Characterization Summary . . . . .	76
4.2	Fitting parameters for different resistivity model-DM19 . . . .	76
4.3	Fitting parameters for different resistivity model-DM24 . . . .	77



# List of Figures

1.1	Resistivity <i>vs.</i> temperature for polycrystalline $\text{SrMg}_x\text{Ru}_{1-x}\text{O}_3$	4
1.2	Magnetization <i>vs.</i> temperature for polycrystalline $\text{SrMg}_x\text{Ru}_{1-x}\text{O}_3$	5
2.1	Guinier Camera-with a Circular Film Holder . . . . .	8
2.2	Sample Guinier photograph $\text{ZnS}$ calibration curve . . . . .	10
2.3	Negative of $\text{SrRuO}_3/\text{ZnS}$ mixture . . . . .	13
2.4	Schematic drawing of the PLD system . . . . .	15
2.5	Wide-range view of the x-ray diffraction pattern-DM9 . . . . .	19
2.6	Expanded view of the x-ray diffraction pattern-DM9 . . . . .	20
2.7	Wide-range view of the x-ray diffraction pattern-DM22 . . . . .	21
2.8	Expanded view of the x-ray diffraction pattern-DM22 . . . . .	22
2.9	Expanded view of the x-ray diffraction pattern-DM20 . . . . .	23
2.10	Expanded view of the x-ray diffraction pattern-DM19 . . . . .	25
2.11	Expanded view of the x-ray diffraction pattern-DM16 . . . . .	26
2.12	Wide-range view of the x-ray diffraction pattern-DM24 . . . . .	27
2.13	Expanded view of the x-ray diffraction pattern-DM24 . . . . .	28
2.14	Expanded view of the x-ray diffraction pattern-DM13 . . . . .	29



---

2.15	Expanded view of the x-ray diffraction pattern-DM15 . . . . .	30
2.16	Expanded view of the x-ray diffraction pattern-DM25 . . . . .	31
2.17	Index (00k) <i>vs.</i> $\sin \theta$ for the DM22 thins film extracted from Fig 2.8 . . . . .	33
2.18	A schematic diagram of the in-plane relationship between (100) <sub>SRO</sub> and (110) <sub>STO</sub> [8] . . . . .	34
3.1	Hysteresis Loop-Polycrystalline SrRuO <sub>3</sub> . . . . .	43
3.2	Hysteresis Loop-Polycrystalline SrMg <sub>0.15</sub> Ru <sub>0.85</sub> O <sub>3</sub> . . . . .	44
3.3	Remanent moment <i>vs.</i> temperature for polycrystalline samples	45
3.4	Inverse magnetization <i>vs.</i> temperature including a linear fit in the range between 245K and 295K . . . . .	46
3.5	Magnetic moment <i>vs.</i> Field for substrates at 5K . . . . .	47
3.6	Magnetic moment <i>vs.</i> temperature at 6 gauss for SrTiO <sub>3</sub> sub- strate . . . . .	48
3.7	Magnetic moment <i>vs.</i> field at T=5K for SrTiO <sub>3</sub> substrate . . .	49
3.8	Hysteresis loop-SrMg <sub>x</sub> Ru <sub>1-x</sub> O <sub>3</sub> thin films grown in O <sub>2</sub> . . . . .	50
3.9	Hysteresis loop-SrMg <sub>x</sub> Ru <sub>1-x</sub> O <sub>3</sub> thin films grown in Ar . . . . .	51
3.10	Comparing moment <i>vs.</i> temperature in 5000G field for Sub- strate and DM19 . . . . .	52
3.11	Thin film moment <i>vs.</i> applied field at 5 K-DM24 . . . . .	53
3.12	Remanent moment <i>vs.</i> temperature of DM9, DM22 and DM24 at zero field . . . . .	54



---

4.1	A schematic representation of different scattering mechanisms which make up total resistivity [25] . . . . .	57
4.2	Simple band picture for Conduction and Valence band in Semiconductor and Insulators. . . . .	58
4.3	Simple band picture for Conduction and Valence band in insulators with impurities . . . . .	59
4.4	Simple band picture for Conduction and Valence band, Anderson Transition . . . . .	61
4.5	Thin film contacts . . . . .	64
4.6	Resistivity <i>vs.</i> Temperature for Pure SrRuO <sub>3</sub> Thin Film (effect of substrate temperature) . . . . .	68
4.7	Effect of O <sub>2</sub> Pressure on Resistivity of SrRuO <sub>3</sub> Thin Films at 500°C . . . . .	69
4.8	Effect of Mg doping on Resistivity in SrMg <sub>x</sub> Ru <sub>1-x</sub> O <sub>3</sub> Thin Films grown in O <sub>2</sub> at 500°C . . . . .	70
4.9	Effect of Mg doping on resistivity for SrMg <sub>x</sub> Ru <sub>1-x</sub> O <sub>3</sub> Thin Films Grown in 200 mtorr Ar Pressure, at 500°C . . . . .	71
4.10	Effect of Mg doping on resistivity for SrMg <sub>x</sub> Ru <sub>1-x</sub> O <sub>3</sub> Thin Films Grown in O <sub>2</sub> Pressure and 600°C . . . . .	72
4.11	Resistance <i>vs.</i> Temperature for DM24 Thin Films Grown in 200 mtorr O <sub>2</sub> Pressure, at 500°C . . . . .	73
4.12	Effect of substrate temperature on SrMg <sub>0.05</sub> Ru <sub>0.95</sub> O <sub>3</sub> and SrMg <sub>0.1</sub> Ru <sub>0.9</sub> O <sub>3</sub> thin films . . . . .	74



---

4.13 Resistivity fit in low temperature range for DM19/24 (activated mobility) . . . . .	77
4.14 Resistivity fit in low temperature range for DM19/24 (variable range hopping) . . . . .	78
4.15 Resistivity fit in low temperature range for DM19/24 (variable range hopping with Coulomb repulsion) . . . . .	79



# Acknowledgements

I would now like to take this opportunity to thank all who have supported me over last couple of years. I am very grateful to my supervisor Dr. David Crandles for giving me a chance to work with his guidance and under his supervision. I appreciate his patience as well. I would also like to thank my committee advisor members Prof. Bose and Dr. Sternin for their helpful recommendations during last two years. I wish to acknowledge Prof. F. S. Razavi for all his support, advice, and help since I arrived in Canada. I especially thank him for allowing me to use his lab and perform most of experiments in there. I would like express my appreciation to all faculty of the Physics Department at Brock University, the guys in the machine shop, electronic shop, and the glass blower who were quick to help me and offering advice.

And finally I thank my father and mother who have encouraged me throughout my studies, and they cannot be credited highly enough.

I dedicate this thesis to Saeed Mahabadi whom I will miss forever.



# Chapter 1

## Introduction

A variety of applications for different ferromagnetic substances in computer memories, electronic and spintronic instruments was the main motivation for further understanding metal-insulator transition and therefore thin film preparation of  $\text{SrRu}_{1-x}\text{Mg}_x\text{O}_3$ .  $\text{SrRuO}_3$  was reported [1, 27, 23, 24] as an itinerant ferromagnet ( $T_c$ =Curie temperature $\sim 160^\circ\text{K}$ ) and it has been widely studied either as a polycrystal or a thin film grown on  $\text{SrTiO}_3$ ,  $\text{MgO}$ , and  $\text{LaAlO}_3$  substrates at least for the last ten years [2, 4, 8, 17, 18]. The ferromagnetic order of  $\text{SrRuO}_3$  at low temperature results from  $4d$  electrons based primarily on the Ru site [2]. It is one of the highly conductive metallic oxides, and it has good thermal conductivity and stability and high resistance to chemical corrosion [3]. Its easy epitaxial growth on various perovskite substrates makes it suitable for multilayer device applications [22].  $\text{SrRuO}_3$  is metallic and belongs to the ternary ruthenium oxide compound family that includes  $\text{BaRuO}_3$  and  $\text{Sr}_2\text{RuO}_4$  [24]. It belongs to the space group of  $Pbnm$  (62), with nearly cubic perovskite structure (orthorhombic) [27] and its lattice parameters are determined to be  $a=0.5570$  nm,  $b=0.5530$  nm, and  $c=0.7856$  nm. [14].



Probing the effects of various dopants in  $\text{SrRuO}_3$  has been under investigation for a long time. There is research on  $\text{SrRuO}_3$  thin films [2, 3, 8, 17, 18]  $\text{Sr}_{1-x}\text{Ca}_x\text{RuO}_3$  and  $\text{SrRu}_{1-x}\text{Ti}_x\text{O}_3$  thin films [2], and  $\text{SrRu}_{1-x}\text{Pb}_x\text{O}_3$  as a polycrystalline material [5].

The table 1.1 illustrates some of the thin films, which have been examined so far.

Thin film	Mag, Increasing $x$	Res.b	Ref
$\text{SrRuO}_3$	F.M	Metallic behaviour	[2, 3, 18]
$\text{Sr}_{1-x}\text{Ca}_x\text{RuO}_3$	F.M, $T_c$ decreases	increasing resistivity	[2]
$\text{SrRu}_{1-x}\text{Ti}_x\text{O}_3$	$T_c$ decreases	M-S transition	[2]

Table 1.1: Thinfilms, a summary of previous work  
 ,Mag:Magnetization, Res.b:Resistivity behaviour,  
 F.M:Ferromagnetic, M-S:Metal to Semiconductor

The effect of Mg doping also has been studied recently by making polycrystalline samples of  $\text{SrRu}_{1-x}\text{Mg}_x\text{O}_3$  synthesized from  $\text{SrCO}_3$ ,  $\text{RuO}_2$ , and  $\text{MgCO}_3\text{Mg}(\text{OH})_2\cdot 3(\text{H}_2\text{O})$  [6]. It was reported the  $\text{Mg}^{+2}$  goes into the  $\text{Ru}^{+4}$  site and that there is a transition from metal to insulator. As long as the amount of Mg is less than  $x = 0.15$ , there is no significant variation in the structure compared to  $\text{SrRuO}_3$  [6].

The data for resistivity versus temperature in magnesium-doped samples show a transition from metallic behaviour at  $x = 0.0$  to insulating behaviour



at  $x = 0.1$  (Fig. 1.1) [6]. Measurements of magnetization show a ferromagnetic phase for  $T < T_c$  and a paramagnetic phase for temperature greater than 160 K (Fig 1.2). Comparison of Figures 1.1 and 1.2 illustrates that even after doping, ferromagnetism persists. Apparently Mg doping produces a transition from a ferromagnetic metal to a ferromagnetic insulator.

The data of Fig. 1.1 show that the temperature dependence of the resistivity is not consistent from batch to batch. The behaviour of the  $x=0.05$  sample is different in 1.1(a) and 1.1(b). This may be due to poor inter-grain connections in low density ceramic samples.

The goal of this thesis is to make epitaxial thin films of the  $\text{SrRu}_{1-x}\text{Mg}_x\text{O}_3$  system by using the laser ablation method and to study the structural, electrical and magnetic properties of the films. The hope was that if epitaxial films could be grown, inter-grain connection problems could be avoided, and resistivity data collected, leading to an insight as to why the metal-insulator (MI) transition occurs. For example, as will be explained in chapter 4, the temperature dependence of resistivity is different depending on whether the MI transition is produced by disorder or by a change in the band structure.

We present our thesis in three major chapters. Chapters 2 and 3 deal with the making of  $\text{SrRu}_{1-x}\text{Mg}_x\text{O}_3$  thin films by laser ablation, and characterization of the films by x-ray diffraction and magnetic measurements. Studying and analyzing the temperature dependence of the resistance in order to understand the metal-insulator transition makes up chapter 4.



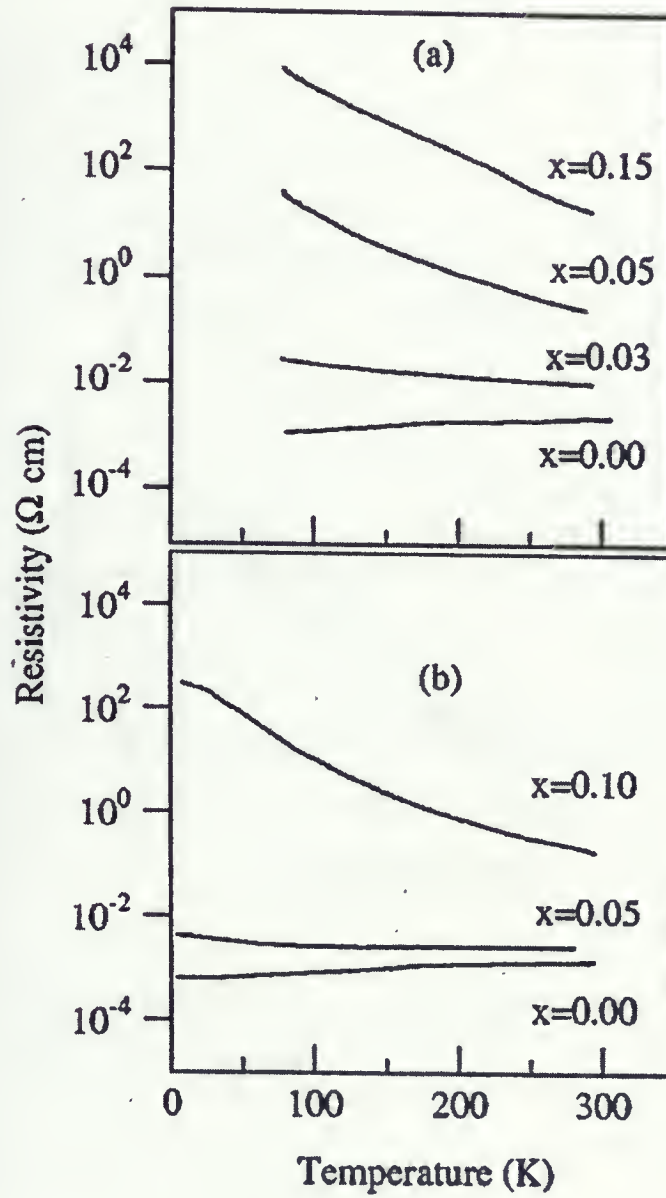


Figure 1.1: Resistivity vs. temperature for polycrystalline  $\text{SrMg}_x\text{Ru}_{1-x}\text{O}_3$  [6]



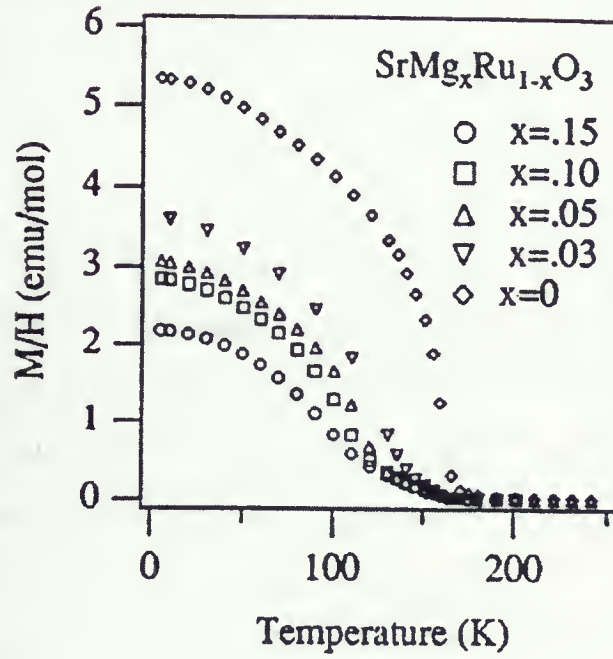


Figure 1.2: Magnetization *vs.* temperature for polycrystalline  $\text{SrMg}_x\text{Ru}_{1-x}\text{O}_3$  [6]



## Chapter 2

# Ablation Targets and Thin Films

The procedure for making the samples is the main part of this chapter. Accuracy in the way of the preparing samples had been the first and the most important part of the process.  $\text{SrCO}_3$  (99.994%-metals basis),  $\text{MgO}$  (99.99%-metals basis), and  $\text{RuO}_2$  (Ru typically 74%), which are manufactured by Alfa Aesar (Johnson-Matthey), were used as raw materials to produce  $\text{SrMg}_x\text{Ru}_{1-x}\text{O}_3$  with different  $x$  values. For this experiment  $x$  chosen to be 0.0, 0.05, 0.1, 0.15, 0.2, and 0.25. Before making thin films, it was necessary to make polycrystalline target pellets.

### 2.1 Instruction for making polycrystalline



Appropriate amounts of  $\text{SrCO}_3$ ,  $\text{MgO}$  with  $\text{RuO}_2$  were ball-milled in a container. The powders were shaken for at least one and a half hours. At this point, the mixed powder was put in a pellet with 1.5 cm diameter. Twenty



tons of force for each pellet was applied. Then, they were put in the furnace for 48 hours at 1200°C. After baking, the pellets were reground, repressed and refired to obtain homogeneous samples.

The details of raw material mass ratios are given in table 2.1.

Materials	SrCO <sub>3</sub>	RuO <sub>2</sub>	MgO
SrRuO <sub>3</sub>	1	0.901	-
SrMg <sub>0.05</sub> Ru <sub>0.95</sub> O <sub>3</sub>	1	0.856	0.00823
SrMg <sub>0.1</sub> Ru <sub>0.9</sub> O <sub>3</sub>	1	0.811	0.272
SrMg <sub>0.15</sub> Ru <sub>0.85</sub> O <sub>3</sub>	1	0.766	0.0409
SrMg <sub>0.2</sub> Ru <sub>0.8</sub> O <sub>3</sub>	1	0.724	0.0546
SrMg <sub>0.25</sub> Ru <sub>0.75</sub> O <sub>3</sub>	1	0.676	0.0682

Table 2.1: Experimental raw material mass ratios for making SrMg<sub>x</sub>Ru<sub>1-x</sub>O<sub>3</sub>

## 2.2 X-ray Diffraction-Guinier Camera

To test for target purity, X-ray Powder Diffraction (XDP) patterns were measured by using a Guinier Camera. Samples were attached to the tape on sample holder, and then mounted in front of the shutter of x-ray beam. Cu K $\alpha$  beam is  $\lambda = 1.5405 \text{ \AA}$ . The exposure time was 5 second for the open Primary Beam Shutter (to expose the reference lines) on the Circular Film Holder and 24 hours for closed one. The optimum Voltage and Current were 25kV and 25mA. After detaching the negative from its place on the camera,



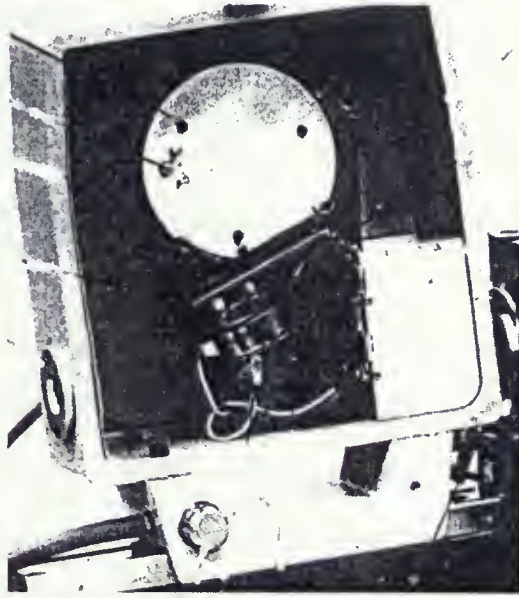


Figure 2.1: Guinier Camera-with a Circular Film Holder

it was washed in distilled water. Each negative was developed and fixed for 5 and 3 minutes, respectively. Figure 2.1 is a picture of the Guinier camera

### 2.2.1 X-ray data for ablation targets

ZnS was chosen as the reference material. It was observed that there were three clear lines belonging to ZnS on the developed negatives [(111), (220), (311)]. ZnS exhibits FCC structure, where  $h$ ,  $k$ , and  $l$  should be all odd or even, and the lattice constant is 5.41 Å [15]. By applying

$$(l^2 + h^2 + k^2)/a^2 = 1/d^2 \quad (2-1)$$



and Bragg's law ( $2d \sin \theta = \lambda$ ) a graph of  $\theta$  vs. distance ( $d$ ) on the film could be made (*e.g.* Fig 2.2). The line position with respect to the zero line and their uncertainties are listed in table 2.2. The slope of Fig 2.2 is used to obtain the rest of the  $\theta$  for  $\text{SrMg}_x\text{Ru}_{1-x}\text{O}_3$ . Note that  $\text{ZnS}/\text{SrMg}_x\text{Ru}_{1-x}\text{O}_3$  mixtures were used for all Guinier photographs.

Figure 2.3 is an example of a developed film which illustrates lines belonging to  $\text{SrRuO}_3$  (SRO) and  $\text{ZnS}$ , but no impurity lines. The indexing (listed in tables 2.3 and 2.4) for  $\text{SrRuO}_3$  was done by comparison to a pattern generated by the program "Crystal Diffract" [7]. Unfortunately certain extra lines on the negative, *e.g.* the 132, 312 splitting, are not distinguishable in these low-resolution Guinier photographs. The data of tables 2.3 and 2.4 show that the  $d$ -spacings do not depend strongly on the magnesium concentration as previously reported [6]. Impurity phases begin to appear for  $x = 0.2$  as there are some unknown lines, which are listed in table 2.3. Hence the  $x = 0.2$  and  $x = 0.25$  sample were abandoned at this stage of the experiment.

Distance (X) in cm	Uncertainty
50.05	$\pm 0.05$
83.45	$\pm 0.05$
99.28	$\pm 0.05$

Table 2.2: Distance of the lines on mixed  $\text{SrRuO}_3/\text{ZnS}$  negative

Considering all of the above points leads us to the following results:



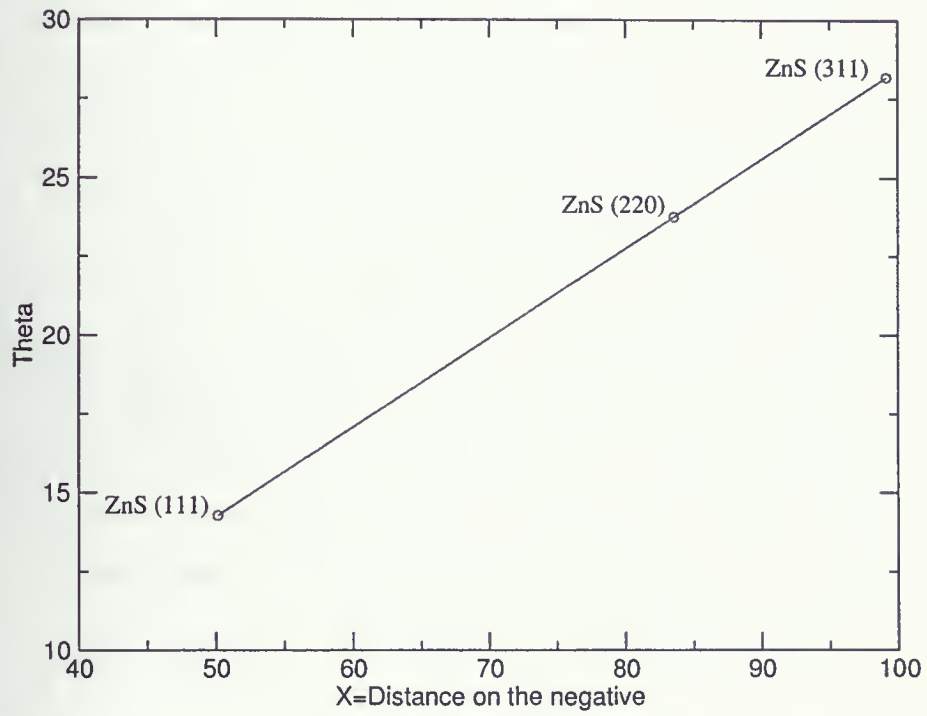


Figure 2.2: Sample Guinier photograph ZnS calibration curve



$x = 0.0$	$x = 0.05$	$x = 0.1$	$(hkl)$
-	-	-	-
$3.938 \pm 0.005$	$3.943 \pm 0.005$	$3.938 \pm 0.005$	(110)
$2.788 \pm 0.002$	$2.782 \pm 0.002$	-	(200)
$2.776 \pm 0.002$	-	$2.779 \pm 0.002$	(112)
-	-	-	-
$1.968 \pm 0.001$	$1.970 \pm 0.001$	$1.971 \pm 0.001$	(220)
$1.962 \pm 0.001$	-	-	(004)
$1.608 \pm 0.0007$	$1.606 \pm 0.0007$	$1.606 \pm 0.0007$	(312)or(132)
$1.390 \pm 0.0005$	$1.389 \pm 0.0005$	$1.394 \pm 0.0005$	(224)
$1.244 \pm 0.0004$	$1.242 \pm 0.0004$	$1.248 \pm 0.0004$	(332)
-	-	-	-

Table 2.3: Table of the  $d$  for spacing on the negatives of  $\text{SrMg}_x\text{Ru}_{1-x}\text{O}_3$



$x = 0.15$	$x = 0.2$	$(hkl)$
-	$4.821 \pm 0.007$	-
$3.944 \pm 0.005$	$3.937 \pm 0.005$	(110)
-	$2.783 \pm 0.002$	(200)
$2.778 \pm 0.002$	-	(112)
-	$2.272 \pm 0.002$	-
$1.968 \pm 0.001$	$1.970 \pm 0.001$	(220)
-	-	(004)
$1.607 \pm 0.0007$	$1.607 \pm 0.0007$	(312)or(132)
$1.394 \pm 0.0005$	$1.390 \pm 0.0005$	(224)
$1.247 \pm 0.0004$	$1.244 \pm 0.0004$	(332)
-	$1.135 \pm 0.0003$	-

Table 2.4: Table of the  $d$  for spacing on the negatives of  $\text{SrMg}_x\text{Ru}_{1-x}\text{O}_3$



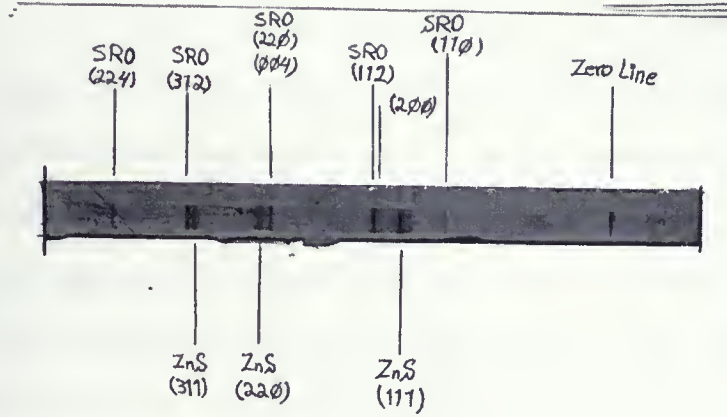


Figure 2.3: Negative of x-ray diffraction result of SrRuO<sub>3</sub>/ZnS mixture

- $d$  spacing obtained from the SrRuO<sub>3</sub> sample is in agreement with previous measurements [6].
- The structure of the pure sample does not change significantly with the magnesium concentration, for  $x \leq 0.15$ .

## 2.3 Pulsed laser deposition

Pulsed laser deposition (PLD) is known as an application of laser ablation for thin film deposition. Figure 2.4 is the schematic diagram of the system used to make all thin films. The type of laser throughout the experiment was *XeCl* with the 308 nm wavelength. The beam of the laser passes through the lenses



to hit the target at the proper place, which is neither in the centre, nor close to the outer edge. Under proper gas pressure, substrate temperature and laser fluence, the film grows epitaxially. One of the mechanisms through which energy can be transferred to the target is called electronic sputtering. There is a group of processes, all of which have the common feature of involving some form of excitation and ionization. The target is struck by the incident photons, which produce electron-hole pairs and an electronic excitation in a very short time. Energy is transferred to the crystal lattice, and in a few ns there is an equilibrium between the electrons and the lattice. This causes a huge heating of the lattice, while irradiation still continues. Therefore a massive particle emission from the surface of the target takes place [11, 9].

These materials are so hot that part of them are ionized. The existence of the laser beam makes them more ionized. By this time a fully ionized plasma is formed. The expansion of the plasma is like the rocket exhaust from jet nozzles, and the visible part of it called the ablation plume. On the other hand oxygen pressure has an influence on the length of the plume, increasing sharpness of the plume boundary, slowing of the plume relative to propagation in vacuum, and some other advantages [11, 9].

### 2.3.1 Thin film-Laser ablation method

SrRuO<sub>3</sub> thin films have been grown by several groups using laser ablation [8, 17] and provided the basic recipe for growing SrRuO<sub>3</sub> (SRO). Nevertheless we studied the effect of the substrate temperature, and of the ambient pressure



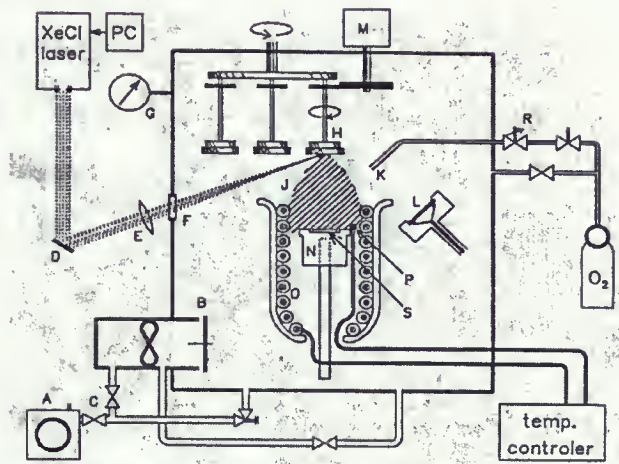


Figure 3.1: Schematic drawing of the PLD system. Legend: A-roughing/backing pump; B-turbomolecular pump with a throttle valve; C-vacuum valves; D-mirror; E-lens; F-quartz window in vacuum chamber; G-vacuum gauge; H-spinning target fastened to target holder on target changer assembly; J-plume of particles ablated from target; K-oxygen gas inlet; L-quartz thickness monitor; M-driving motor for target spinning; N-substrate holder in the heater, fixed on ceramic rod; O-spiral of resistive heating element; P-thermocouple; R-variable leak valve for fine adjustment of  $O_2$  partial pressure; S-substrate on the holder

Figure 2.4: Schematic drawing of the PLD system [34]



on the film quality. When it came to grow Mg, doped samples, the effect of different atmospheres (Ar, and O<sub>2</sub>) were studied because we anticipated difficulty in depositing Mg, as encountered in previous work [33]. The most important problem might be due to chemical reaction between Mg and the oxygen atmosphere during the deposition. Thin films were deposited on (100) SrTiO<sub>3</sub> (STO) substrates by pulsed laser deposition (PLD), using a XeCl laser. SrTiO<sub>3</sub> is one of the most applicable substrates with a perovskite structure and the lattice parameters of  $a = b = c = 3.905 \text{ \AA}$  [8]. Table 2.5 indicates all the thin films and the conditions in which they were made. During deposition of SrRuO<sub>3</sub>, it was noticed that the colour of the plume in O<sub>2</sub> is orange. As the amount of Mg was increased, the colour became yellow-orange, and in Ar atmosphere blueish- yellow was visible. Another significant difference was in the shape of the plume in these two atmospheres. The plume in O<sub>2</sub> was almost a conical shape, but in Ar it was more spherical.

## 2.4 X-ray data for thin films

SrMg<sub>x</sub>Ru<sub>1-x</sub>O<sub>3</sub> thin films were grown on (001) SrTiO<sub>3</sub> (STO) [32]. The diffraction patterns of SrMg<sub>x</sub>Ru<sub>1-x</sub>O<sub>3</sub> (SRO) thin films deposited on STO substrate have been determined by powder x-ray diffraction (XRD) at McMaster University. Two of the films, DM22 and DM24, were characterized by energy dispersive x-ray spectroscopy(EDX). EDX is a microanalytical technique that uses the characteristic spectrum of x-rays emitted by the specimen



S.N	Target	S.T°C	Atmosphere/Pressure	Pulses
DM4	$\text{SrRuO}_3$	600	$\text{O}_2/200$ mtorr	10000
DM5	$\text{SrRuO}_3$	500	$\text{O}_2/200$ mtorr	10000
DM6	$\text{SrRuO}_3$	400	$\text{O}_2/200$ mtorr	10000
DM7	$\text{SrRuO}_3$	500	$\text{O}_2/150$ mtorr	10000
DM8	$\text{SrRuO}_3$	400	$\text{O}_2/200$ mtorr	10000
DM9	$\text{SrRuO}_3$	500	$\text{O}_2/200$ mtorr	10000
DM10	$\text{SrRuO}_3$	600	$\text{O}_2/200$ mtorr	10000
DM11	$\text{SrRuO}_3$	500	$\text{O}_2/250$ mtorr	10000
DM12	$\text{SrMg}_{0.15}\text{Ru}_{0.85}\text{O}_3$	500	$\text{O}_2/200$ mtorr	10000
DM13	$\text{SrMg}_{0.15}\text{Ru}_{0.85}\text{O}_3$	500	$\text{O}_2/200$ mtorr	20000
DM14	$\text{SrMg}_{0.15}\text{Ru}_{0.85}\text{O}_3$	500	$\text{Ar}/200$ mtorr	10000
DM15	$\text{SrMg}_{0.15}\text{Ru}_{0.85}\text{O}_3$	500	$\text{Ar}/200$ mtorr	20000
DM16	$\text{SrMg}_{0.1}\text{Ru}_{0.9}\text{O}_3$	500	$\text{Ar}/200$ mtorr	20000
DM17	$\text{SrMg}_{0.1}\text{Ru}_{0.9}\text{O}_3$	600	$\text{Ar}/200$ mtorr	20000
DM18	$\text{SrMg}_{0.1}\text{Ru}_{0.9}\text{O}_3$	600	$\text{O}_2/200$ mtorr	20000
DM19	$\text{SrMg}_{0.1}\text{Ru}_{0.9}\text{O}_3$	500	$\text{O}_2/200$ mtorr	10000
DM20	$\text{SrMg}_{0.05}\text{Ru}_{0.95}\text{O}_3$	500	$\text{Ar}/200$ mtorr	20000
DM21	$\text{SrMg}_{0.05}\text{Ru}_{0.95}\text{O}_3$	600	$\text{Ar}/200$ mtorr	20000
DM22	$\text{SrMg}_{0.05}\text{Ru}_{0.95}\text{O}_3$	500	$\text{O}_2/200$ mtorr	20000
DM23	$\text{SrMg}_{0.05}\text{Ru}_{0.95}\text{O}_3$	600	$\text{O}_2/200$ mtorr	20000
DM24	$\text{SrMg}_{0.1}\text{Ru}_{0.9}\text{O}_3$	500	$\text{O}_2/200$ mtorr	70000
DM25	$\text{SrMg}_{0.15}\text{Ru}_{0.85}\text{O}_3$	500	$\text{O}_2/200$ mtorr	50000

Table 2.5: Thin film growth parameters, (S.N:Sample Number, S.T:Substrate Temperature)



after an excitation by high-energy electrons to obtain information about its elemental composition [35]. These measurements were done at McMaster University as well.

### 2.4.1 $\text{SrRuO}_3$ thin film-DM9

As one may notice the results of the  $2\theta$  x-ray scan for DM9 show only the  $(00\ell)$  peaks (Fig 2.5, 2.6) , which might be explained by growing the thin film with its  $c$ -axis normal to the substrate surface as in previous reports [8]. No impurity phases appear on the x-ray diffraction pattern for DM9. However the  $\text{SrRuO}_3$  films do not have as good epitaxial quality as in the previous report [8], since the lines have a large value of full-width at half maximum(FWHM).

### 2.4.2 $\text{SrMg}_{0.05}\text{Ru}_{0.95}\text{O}_3$ thin film-DM20/22

By adding Mg the same pattern as pure  $\text{SrRuO}_3$  is obtained. A wide range intensity *vs.*  $2\theta$  graph still confirms no impurity phases for DM22 where the target is  $\text{SrMg}_{0.05}\text{Ru}_{0.95}\text{O}_3$  (Fig 2.7). But there is no clear sign of any diffraction peaks in DM20 (Fig 2.9) as for all the other thin films grown under Ar (Fig 2.9, 2.11 and 2.15). It suggests that the Ar atmosphere might not be a proper environment for epitaxial growth of thin films. It is not clear whether the x-ray data indicate amorphous films or extremely thin films. Unfortunately EDX was not sensitive enough to measure any trace of Mg



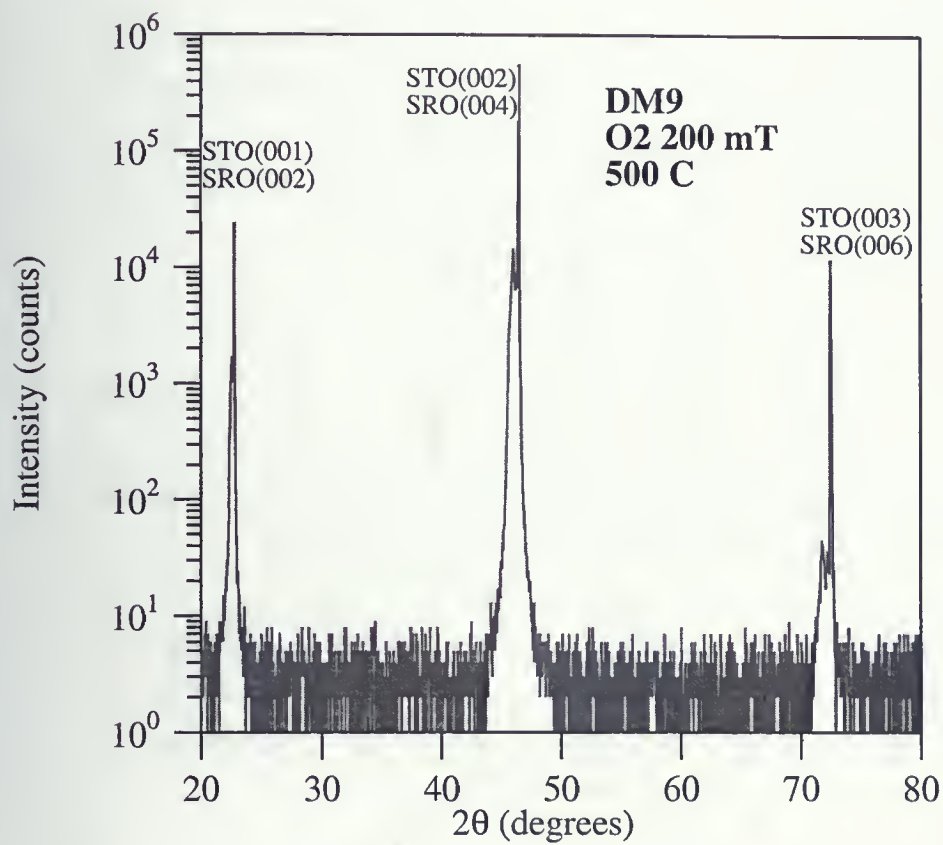


Figure 2.5: Wide-range view of the x-ray diffraction pattern for sample DM9



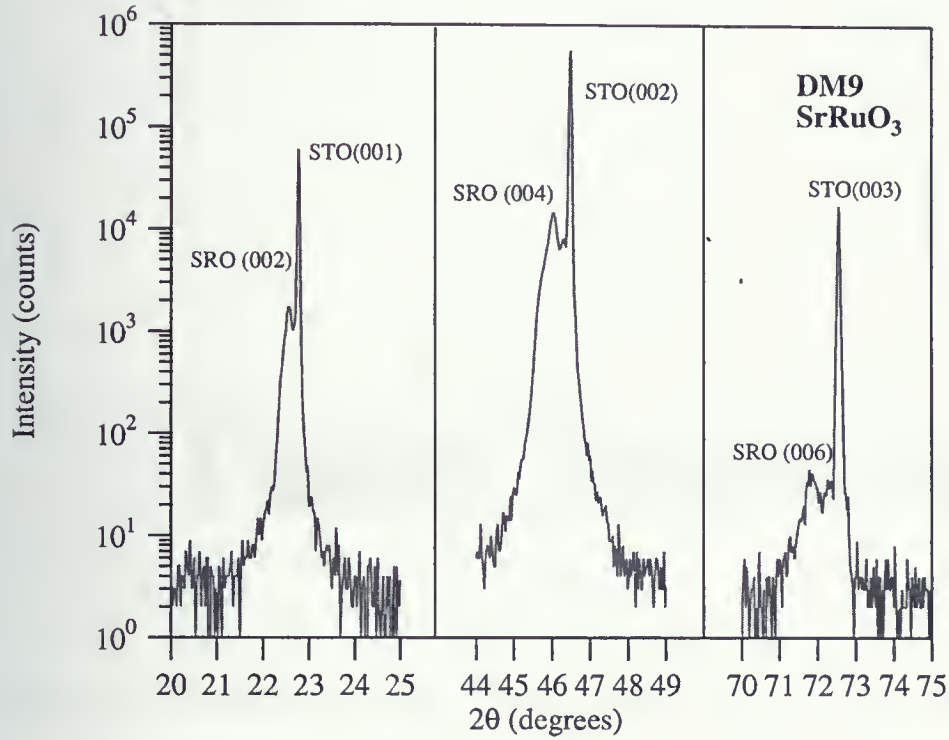


Figure 2.6: Expanded view of the x-ray diffraction pattern for sample DM9



compared to Ru for DM22.

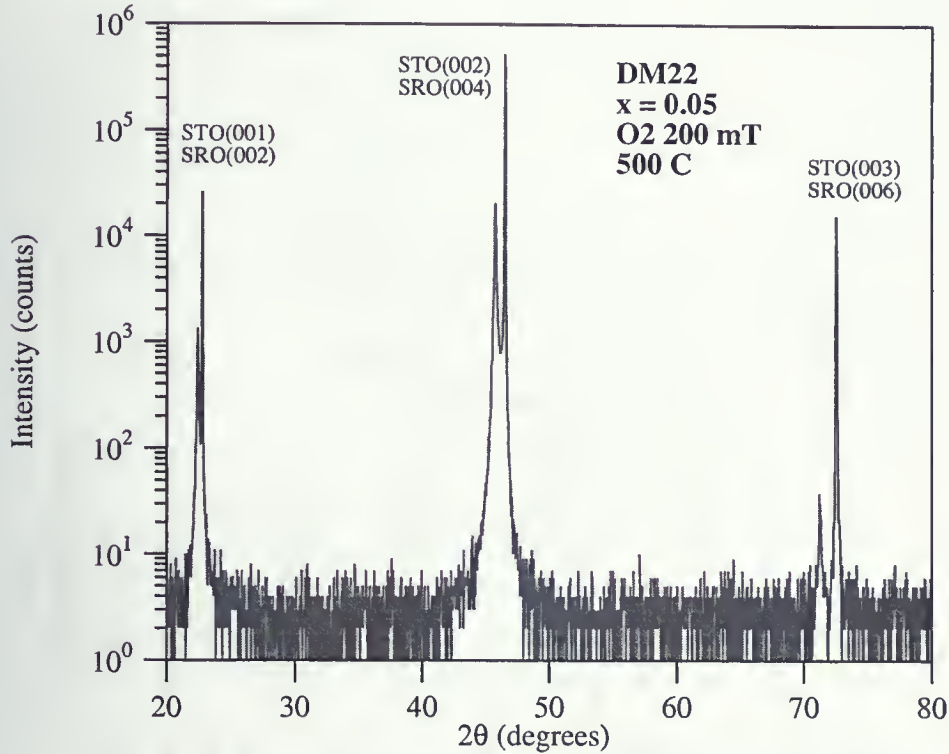


Figure 2.7: Wide-range view of the x-ray diffraction pattern for sample DM22

### 2.4.3 $\text{SrMg}_{0.1}\text{Ru}_{0.9}\text{O}_3$ thin film-DM16 and DM19/24

Another interesting result of x-ray diffraction is in the significance of the thickness of thin films. Sample DM19 (Fig 2.10) and DM24 (Figs 2.12, 2.13) were grown under the same conditions, but with a different number of ablation pulses. The peaks of the SRO for DM24 are more distinguishable in



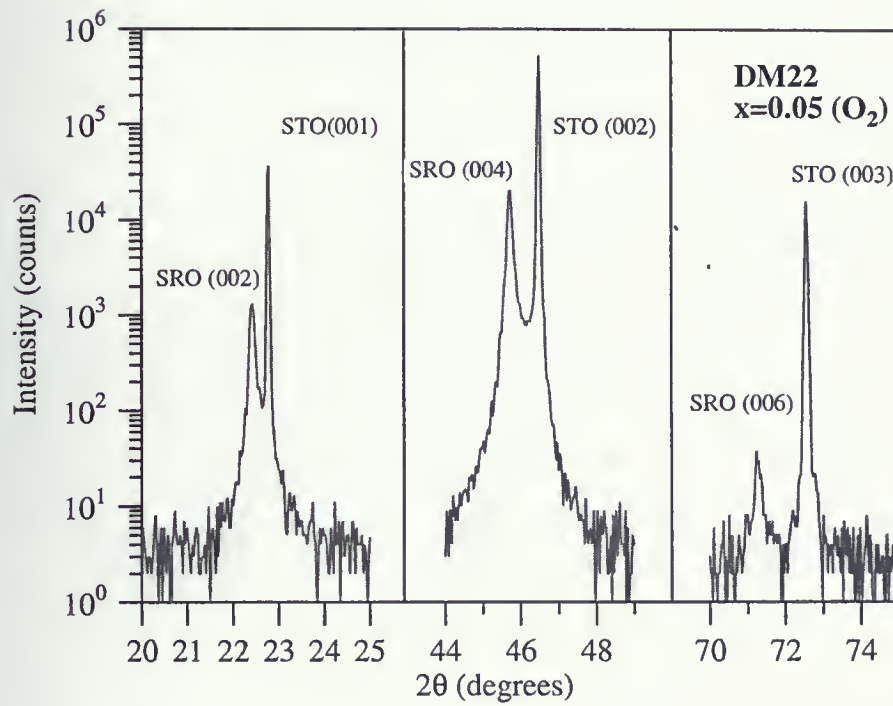


Figure 2.8: Expanded view of the x-ray diffraction for sample DM22



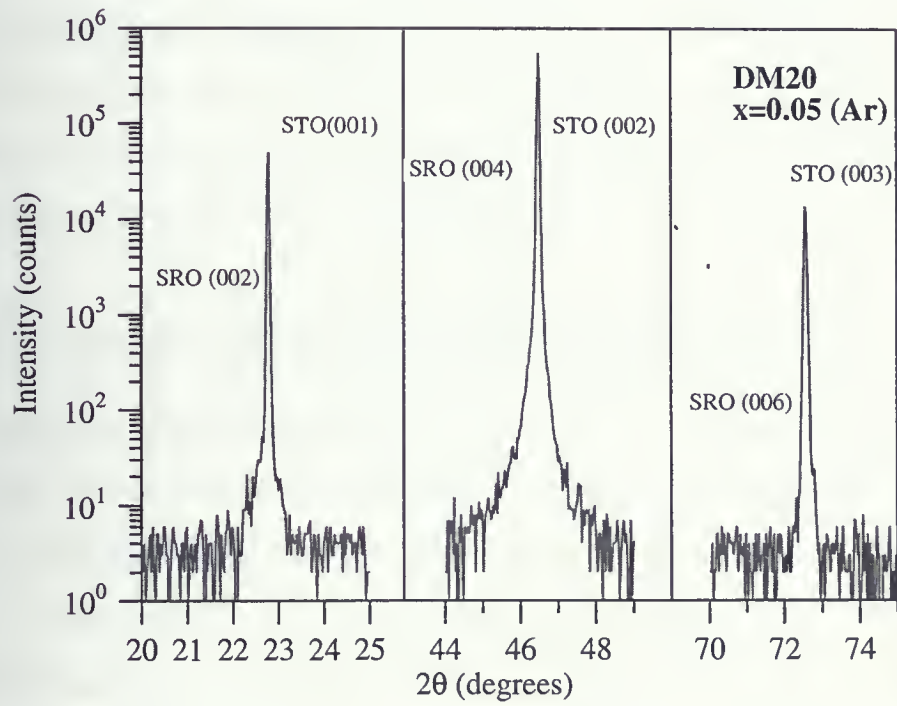


Figure 2.9: Expanded view of the x-ray diffraction for sample DM20



comparison to DM19, since thickness should be proportional to pulse number. But some other lines are exhibited on the wide-range graph of DM24 (Fig 2.12). This is not an epitaxial growth any more, but there are no impurity phases apparent in figure 2.12. EDX measurement for DM24 shows the existence of Mg in the thin film. This result is close to target stoichiometry. The ratio of atomic % Mg/Ru is 0.0855. In other words for every 100 atoms, 8 atoms are Mg and the rest is Ru. X-ray diffraction for DM16 (Fig: 2.11) does not show peaks for SRO, therefore either this sample is too thin or an amorphous film was made on the substrate.

#### 2.4.4 $\text{SrMg}_{0.15}\text{Ru}_{0.85}\text{O}_3$ thin film-DM13/15/25

Figures 2.14 and 2.15 suggest that the chosen growth conditions were not proper for epitaxial growth of  $\text{SrMg}_{0.15}\text{Ru}_{0.85}\text{O}_3$ . In comparison to figure 2.14, figure 2.16 shows that even with more laser pulses there is no evidence of epitaxial growth of the thin film doped with Mg ( $x = 0.15$ ). The sample DM25 was grown by using 50000 pulses compared to 20000 for the sample DM13.

### 2.5 Lattice parameters of thin films

The epitaxial growth of SRO film on STO substrate using laser ablation has been observed before [8]. It has been suggested that  $\text{SrRuO}_3$  grows on (100)  $\text{SrTiO}_3$  such that  $(100)_{\text{SRO}} \parallel (110)_{\text{STO}}$  [8, 18]. Based on the results of XRD



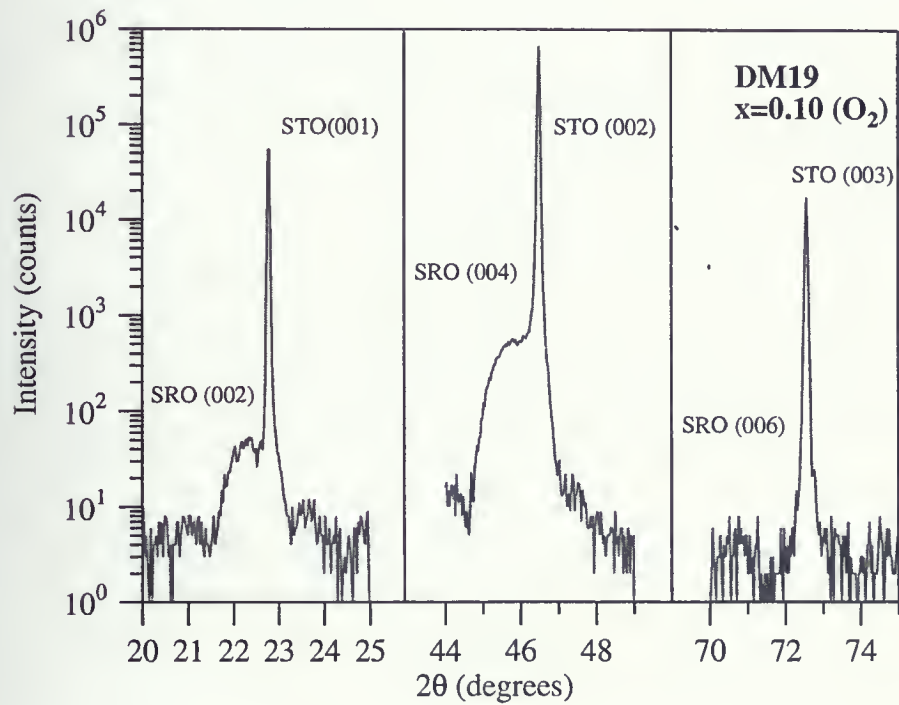


Figure 2.10: Expanded view of the x-ray diffraction for sample DM19



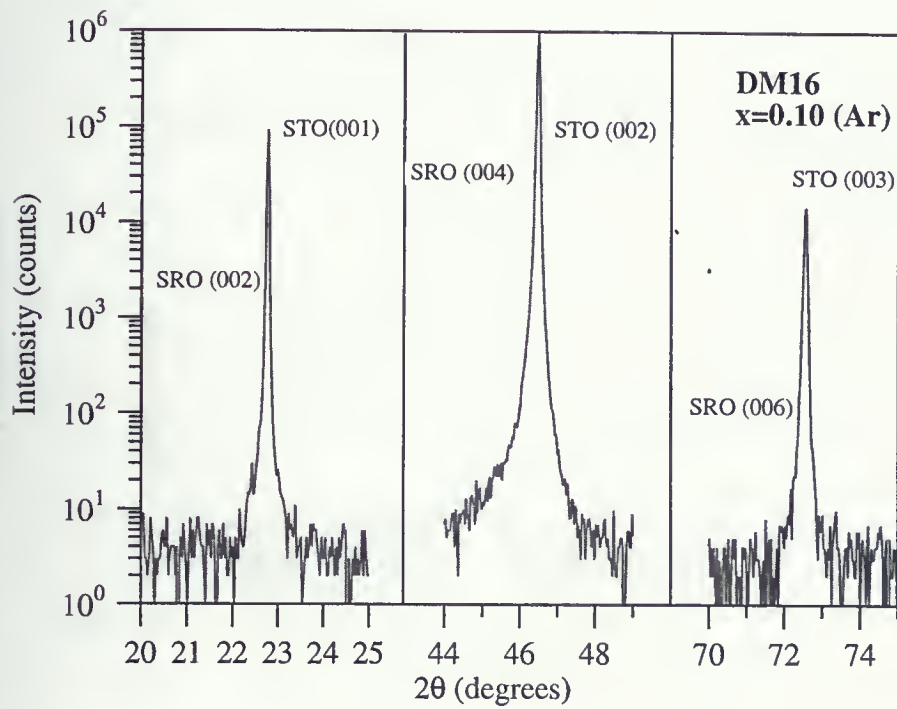


Figure 2.11: Expanded view of the x-ray diffraction for sample DM16



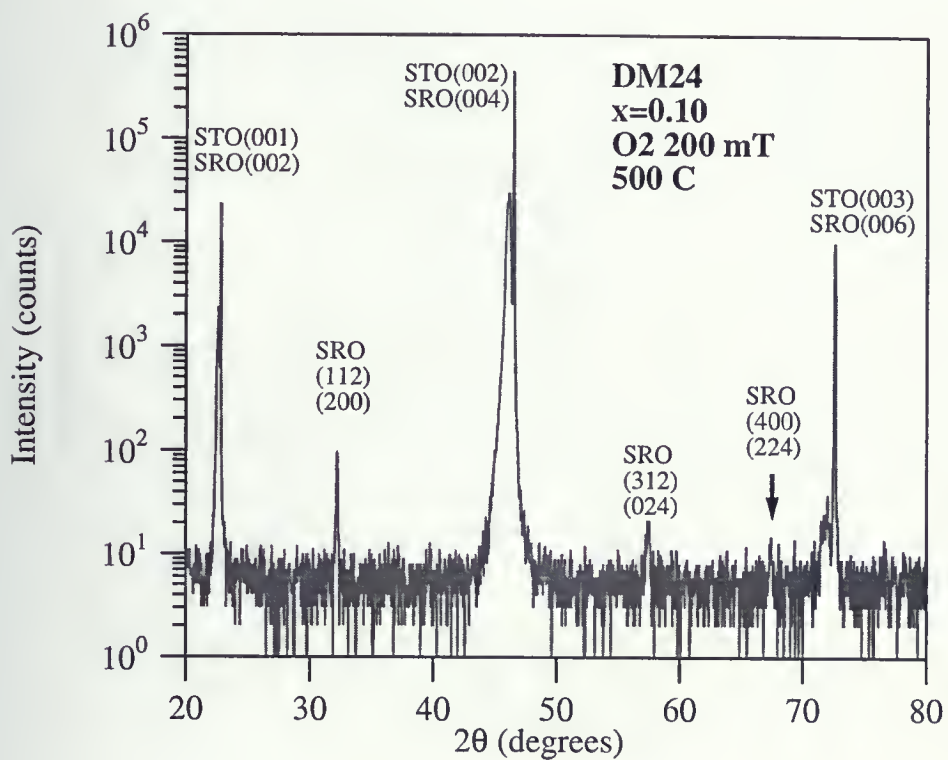


Figure 2.12: Wide-range view of the x-ray diffraction pattern for sample DM24



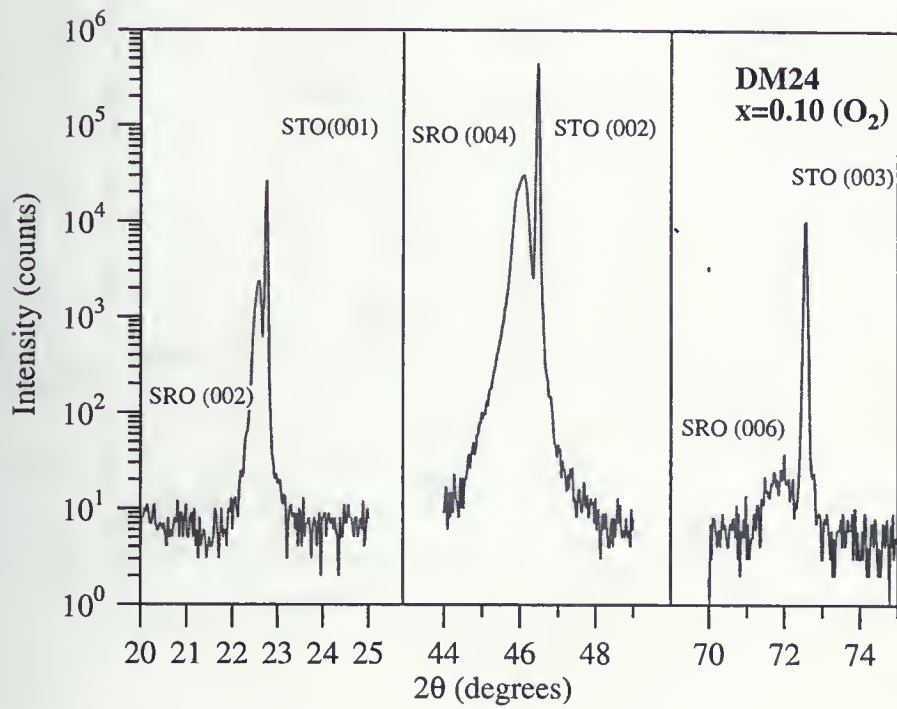


Figure 2.13: Expanded view of the x-ray diffraction for sample DM24



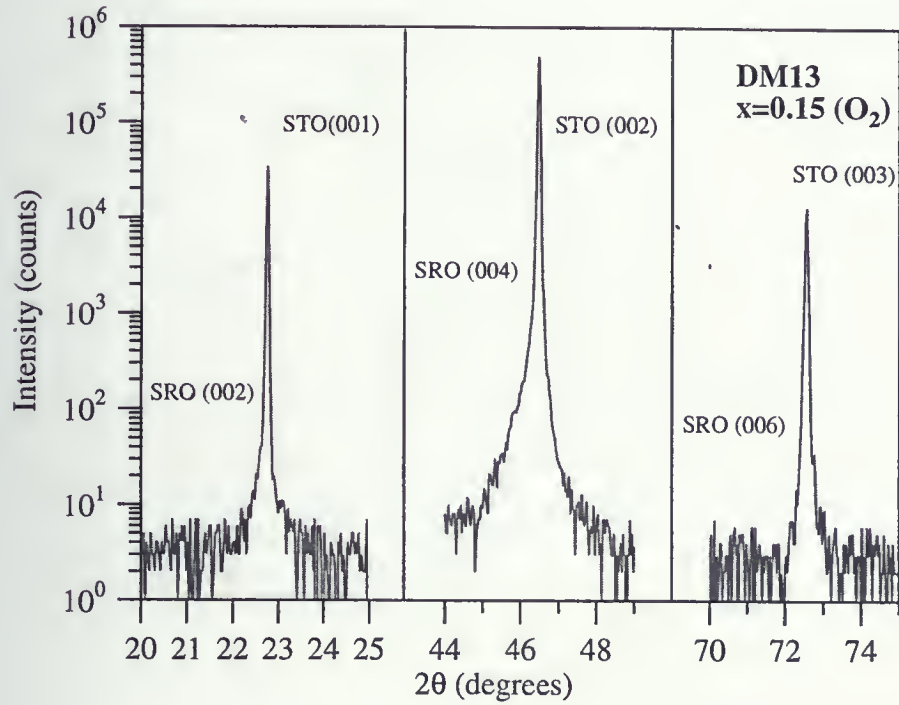


Figure 2.14: Expanded view of the x-ray diffraction for sample DM13



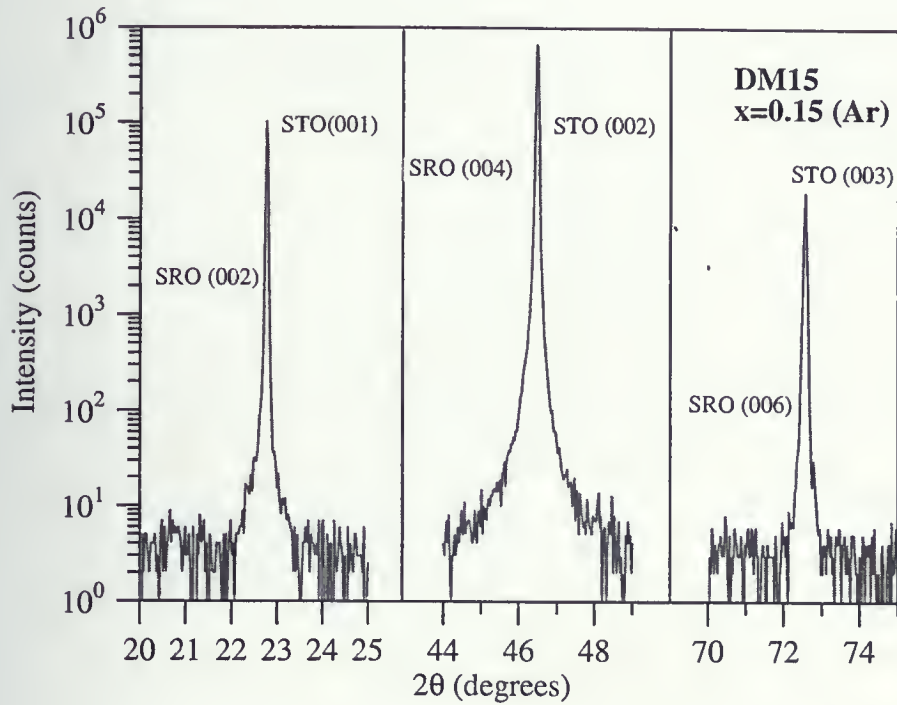


Figure 2.15: Expanded view of the x-ray diffraction for sample DM15



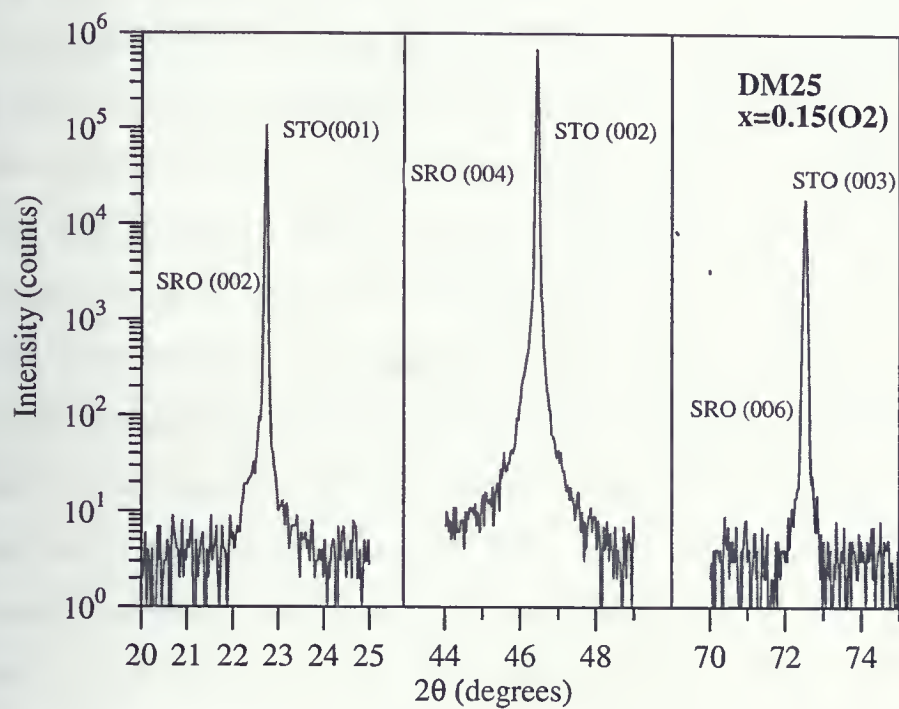


Figure 2.16: Expanded view of the x-ray diffraction for sample DM25



(see figures 2.6, 2.8, 2.10, 2.13) from graphs and using the orthorhombic equation for  $d$  spacing between each plane  $1/d^2 = h^2/a^2 + k^2/b^2 + l^2/c^2$ , the lattice parameter  $c$  of the SRO was determined. For instance, XRD data of Fig 2.8 for DM22 illustrates three  $(00k)$  lines from which a graph of  $k$  vs.  $\sin \theta$  could be constructed (Fig 2.17). From the slope of this graph which is  $\lambda/2c$ , one lattice parameter of SRO,  $c$ , could be determined. The results are listed in table 2.6. The lattice constant of cubic STO is  $a=3.905 \text{ \AA}$ . The  $(110)$  diagonal shown in 2.18, which parallel to the  $(100)$  of SRO, is therefore  $5.523 \text{ \AA}$ , which is shorter than either  $a=5.57 \text{ \AA}$  or  $b=5.53 \text{ \AA}$ , the lattice parameters of pure polycrystalline  $\text{SrRuO}_3$  [8]. Hence there should be a natural compressive strain of about 0.5% in the  $a, b$  plane of the SRO thin films tending to make the  $c$ -axis of the films longer. If the volume of the SRO cell were to remain constant at  $(5.53)\text{\AA} \cdot (5.57)\text{\AA} \cdot (7.85)\text{\AA} = 241.8\text{\AA}^3$ , then one would expect the  $c$ -parameter of epitaxial films to be  $241.8/(5.523)^2 = 7.93\text{\AA}$  which is close to the value found for DM22 as table 2.5 indicates. As seen in Fig 2.8, 2.10 and Fig 2.13, the film DM22 has the best epitaxial quality of all the films examined as evidenced by the narrowest of the diffraction peaks.



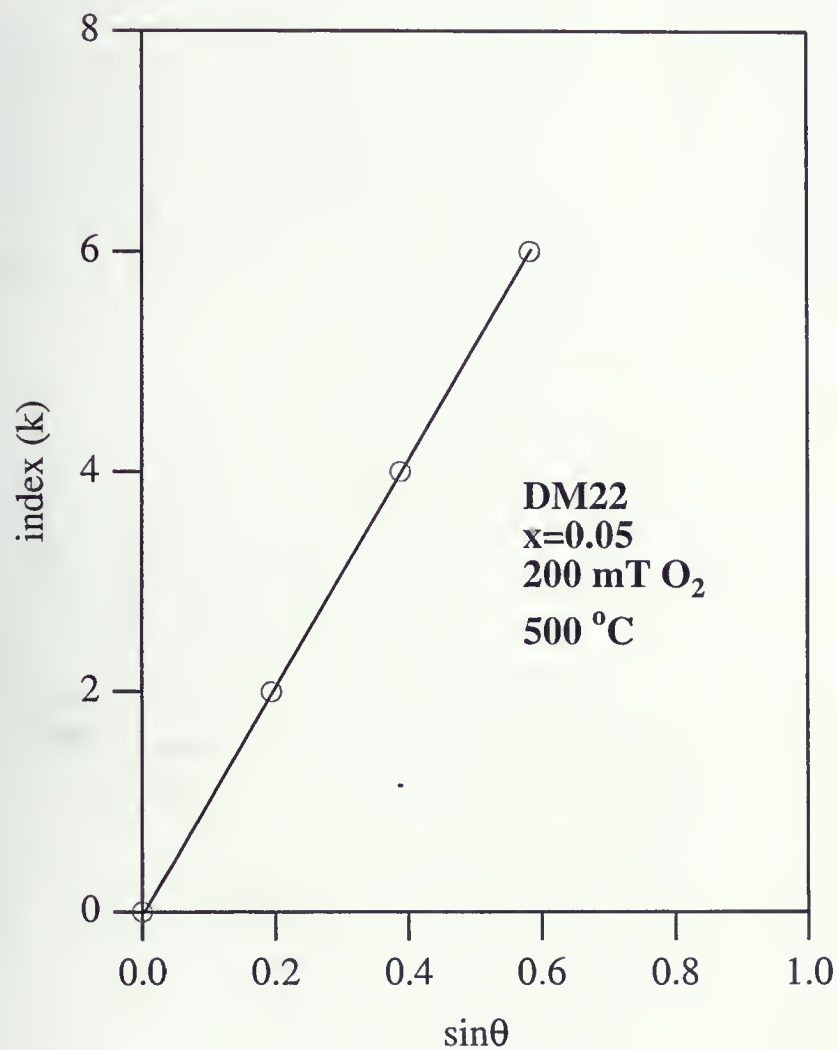
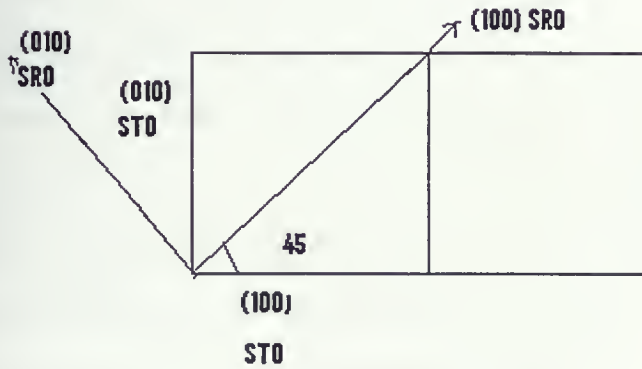


Figure 2.17: Index (00k) *vs.*  $\sin\theta$  for the DM22 thin film extracted from Fig 2.8



Thin Film	$c$	$x$	Number of pulses
DM9	$7.853 \pm 0.0015$	0	10000
DM22	$7.931 \pm 0.003$	0.05	20000
DM19	$7.89 \pm 0.05$	0.1	20000
DM24	$7.875 \pm 0.002$	0.1	70000

Table 2.6: Lattice parameters of SRO thin films on a STO substrate

Figure 2.18: A schematic diagram of the in-plane relationship between  $(100)_{SRO}$  and  $(110)_{STO}$  [8]



# Chapter 3

## Magnetization

### 3.1 Magnetism in metals and insulators

#### 3.1.1 Paramagnetism and Ferromagnetism

The simple semi-classical explanation for paramagnetism of a set of non-interacting spins is as follows [19]: The magnetic dipole moment  $\mu$  is determined by the current of an electron multiplied by the area around which electron rotates. The angular momentum is  $L = mr^2\omega$ , where  $\omega$  is the angular velocity. For one electron we can easily show that the current is equal to  $e(\omega/2\pi)$  and the area of the loop is  $\pi r^2$ . Therefore the relation between angular momentum and magnetic moment is  $\mu = (-e/2m)L$ . There is also a magnetic moment associated with the spin, which is  $\mu = (-e/m)S$ . The magnetic moment  $\mu$  can be expressed in terms of the total angular momentum  $J$  as  $\mu = g(-e/2m)J$ , where  $g$  is gyromagnetic or magnetogyric ratio. To calculate the magnetization of a doubly degenerate  $J = 1/2$  states one considers the different populations in the Zeeman split states. In the presence of an applied field, degenerate energy levels are split by the Zeeman



energy  $E = -\mu \cdot B = g\mu_B B m_j$ .  $\mu_B$  is called Bohr magneton and if  $J = 1/2$ ,  $m_j$  is  $1/2$  or  $-1/2$  resulting in a double splitting. The magnetization is given by  $M = g\mu_B(N_1 - N_2)$ , where  $N_1$  and  $N_2$  are the number of atoms per unit volume in the lower and upper levels, respectively. As the magnetic field becomes larger, the spacing between the levels increases and the dipoles drop from higher to the lower level, leading to net magnetization. This magnetization is induced by the field, which can be an internal field, and has the relation as  $M = \chi_p H$ , where  $\chi_p = C/T$ . [19]. The spontaneous magnetization in transition metals (Fe, Ni), rare-earth elements (Gd, Dy) and in transition metal oxides such as  $\text{CrO}_2$  and  $\text{SrRuO}_3$  is called ferromagnetism. It is due to interactions between neighboring spins. Finding this property in transition and rare-earth elements indicates that it is related to the unfilled 3d and 4f shells in these substances [19]. Ferromagnetism appears below a certain temperature, which is called the Curie temperature  $T_c$  or the ferromagnetic transition temperature. At temperatures above  $T_c$  the substance is paramagnetic and the magnetic susceptibility is given by the Curie-Weiss law.

### 3.1.2 The Curie-Weiss Model

This model describes the magnetization in the paramagnetic state with localized spins. The Curie Law for a simple paramagnet is  $\chi_p = C/T$  [Eq.1]. In a material with  $N$  atoms of spin  $S$ , one assumes the spins tend to line up parallel to each other and the Exchange Field  $B_E$  [15].



$B_E$  is assumed proportional to magnetization:  $B_E = \lambda M$  where  $\lambda$  is a constant and independent of temperature. At  $T_c$  and above (paramagnetic phase) the spontaneous magnetization vanishes. If we applied one magnetic field,  $B_a$  and considering  $\chi_p$  as paramagnetic susceptibility, magnetization is obtained by:

$$M = \chi_p(B_a + B_E) \quad (3.2)$$

By substituting Eq.1 into Eq.2 we have:

$$\chi = M/B_a = C/(T - C\lambda) \quad (3.3)$$

In the latter equation,  $C$  is called Curie-Weiss constant while  $T_c = C\lambda$ . This constant is obtained from the following formula:

$$C = N\mu_{eff}^2/3k_B$$

$N$  is the number of effective spins in the sample, which in this case is  $Ru^{+4}$ .  $\mu_{eff}$  is the effective moment per magnetic atom in the paramagnetic state.

If such a ferromagnet with localized spins were placed in an external magnetic field below  $T_c$ ,  $M$  would increase until all the spins were aligned, a condition called saturation.

### 3.1.3 Ferromagnetism in Insulators

In an insulator the spins are localized on the atomic sites. Above the Curie temperature the moments are oriented randomly, resulting in a zero field net magnetization and in this region the substance is paramagnetic [19]. Below



$T_c$  the internal exchange interaction between neighboring moments tends to line them up parallel to each other.

### 3.1.4 Ferromagnetism in metals - itinerant model

The magnetic property of delocalized electrons can be explained by the itinerant-electron model: The electrons in a band divide into two spin sub-bands, up and down. Considering magnetic energy,  $E = -\mu \cdot B$ , where  $\mu$  is the magnetic moment, electrons tend to go to the lower energy, so if the internal  $B$  is in z-direction so electrons move from the down to the up direction and as result there exists a net magnetization and therefore ferromagnetism [19]. Ferromagnetic metals also obey the Curie-Weiss law above  $T_c$ , however it is not fully understood yet why. By looking at equation (3.3), one can say as temperature is lowered to  $T_c$ ,  $\chi$  diverges. In the temperature range  $T < T_c$ , magnetization can also be saturated by applying a large enough field. The saturation moment is represented by  $\mu_s$ . A method for distinguishing between localized and itinerant ferromagnetic material is to consider the ratio of  $\mu_{eff}/\mu_s$ .  $\mu_{eff}$  is the effective moment per atom in the paramagnetic state.  $\mu_s$  is the effective moment per atom in the ferromagnetic state as determined from the saturation magnetic atom. For a localized ferromagnetic material,  $\mu_{eff}/\mu_s$  is one or close to one. If the ratio is more than one, the material is an itinerant ferromagnet [12].



## 3.2 Procedure and discussion

The SQUID detection system (Model MPMS/MPMS2-Quantum Design), was used to explore the magnetic properties of  $\text{SrMg}_x\text{Ru}_{1-x}\text{O}_3$ . Here, polycrystalline pellets, substrates, and thin films were under investigation. First we observed the results of polycrystalline samples. The magnetization of  $\text{SrMg}_x\text{Ru}_{1-x}\text{O}_3$  pellets was measured as follows: The samples were cooled down to 5K in zero field, then hysteresis curves were measured (*e.g.* Fig 3.1, Fig 3.2). After that remanent moments at almost zero field were established. We measured the remanent moment versus temperature till 170K. Finally the applied field was increased to 1000 G, and the moment measured for  $180\text{K} \leq T \leq 300\text{K}$  in the paramagnetic state.

### 3.2.1 Magnetic properties of polycrystalline

#### $\text{SrMg}_x\text{Ru}_{1-x}\text{O}_3$

In this study we measured the magnetic properties of polycrystalline samples. Hysteresis loops of polycrystalline samples were plotted at very low temperature (Figures 3.1, 3.2). Magnetization increases rapidly with an increase in the magnetic field since the measurement is at temperature much lower than  $T_c$ . The maximum magnetization decreases from pure  $\text{SrRuO}_3$  to  $\text{SrMg}_{0.15}\text{Ru}_{0.85}\text{O}_3$ . The maximum external field for these experiments was 5T, but even in 44T there is no evidence of magnetic saturation for  $\text{SrRuO}_3$  [31], hence it was not possible to measure  $\mu_s$ . In figure 3.3 the remanent mag-



netization versus temperature is illustrated. Note the similarity to previous measurements shown in Fig 1.2. But Mg has an effect on the ferromagnetic and paramagnetic phases. The temperature dependence of the inverse magnetic susceptibility in the paramagnetic phase (well above the Curie temperature) is shown in figure 3.4. The effective moments per Ru atom,  $\mu_{eff}$ , for polycrystalline pellets of  $\text{SrMg}_x\text{Ru}_{1-x}\text{O}_3$ , where  $x = (0.0, 0.05, 0.1, 0.15)$ , were calculated from fits to  $\chi = M/B_a = C/(T - T_c)$ . The slope of figure 3.4 is equal to  $3Nk_B\mu_{eff}^2$ . This calculation leads us to figure out  $\mu_{eff}$ . The effective moment per magnetic atom shows a systematic decrease from  $3.12\mu_B$  for  $x = 0.0$  to  $2.2\mu_B$  for  $x = 0.15$  as listed in table 3.1. Those results are similar to previously reported data [6].

### 3.2.2 Magnetic properties of $\text{SrTiO}_3$ substrate

The response of the  $\text{SrTiO}_3$  substrate became significant during the experiment particularly when the thickness of thin films was very small. For this reason the magnetic property of the substrates were investigated. The susceptibility of an insulating crystal consists of a pure diamagnetic term and a term representing paramagnetism [30]. At 5K the moment of two substrates versus applied field were measured (Fig 3.5). The mass of these two substrates are similar to each other (0.13 and 0.12898 gr). The result confirms that  $\text{SrTiO}_3$  is a diamagnetic material. On the other hand between 0 up to 1000 gauss magnetization contains some positive numbers, which is a sign of paramagnetic impurities in substrates. Figure 3.6 illustrates magnetization



versus temperature at very low field. Note the hysteresis: the response is different depending on whether temperature increases or decreases. We do not understand the hysteresis. It is unlikely to be due to condensed solid oxygen which should have a peak near the  $\gamma$ - $\beta$  transition at 44K [37]. The hysteresis loop of SrTiO<sub>3</sub> (Fig 3.7) shows the effect of the paramagnetic impurity in region between -1000 gauss up to 2000 gauss. As will be seen, the magnetic response of the substrate must be considered when understanding the measurement on some films.

### 3.2.3 Magnetic properties of SrMg<sub>x</sub>Ru<sub>1-x</sub>O<sub>3</sub> thin films

The effect of Mg substitution is remarkable in SrMg<sub>x</sub>Ru<sub>1-x</sub>O<sub>3</sub> thin films. As one may notice by looking at figure 3.8, the hysteresis loops for thin films grown in O<sub>2</sub> atmospheres show a systematic decrease in magnetization as the amount of Mg increases in SrMg<sub>x</sub>Ru<sub>1-x</sub>O<sub>3</sub>. For thin films grown in Ar the results are different (Fig 3.9). Comparing Fig 3.9 and Fig 3.8 with Fig 3.1 one sees that the thin film signal is strongly affected by the substrates. The magnetic data of figure 3.9 is consistent with the lack of diffraction peaks in Fig. 2.9, 2.11. and 2.15. It is evidence that good films can not be grown in Ar. Fig. 3.10 is interesting. It compares the magnetic moment of a thin film sample grown in O<sub>2</sub> (DM19) as a function of temperature with that of a substrate on its own. The moments were measured while cooling the samples from 300K to 90K in a 5000G field. Although the x-ray data (Fig 2.10) suggest the presence of SrMg<sub>x</sub>Ru<sub>1-x</sub>O<sub>3</sub> in DM19, the film must



be very thin as there is no trace of ferromagnetism. It can be concluded from Fig 3.8, 3.9, and 3.10 that film signals for DM13, DM15, and DM 19 are too small. On the other hand DM24 is a much thicker  $x=0.1$  film. As discussed in chapter 2 it is not epitaxial, but it does show similar hysteresis curve data to the polycrystalline target (Fig 3.11). The results of XRD for DM9, DM22, and DM24 indicate a distinguishable peak for SRO, and are consistent with results of remanent moment measurements (Fig 3.12). We cannot compare the different data in Fig 3.12 with each other because the thickness of the films are unknown and probably different as the number of pulses is different.

$\mu_{eff} \pm \delta\mu_{eff}$	$x$
$3.12 \pm 0.014$	0.0
$2.54 \pm 0.012$	0.05
$2.42 \pm 0.016$	0.1
$2.20 \pm 0.014$	0.15

Table 3.1: Number of  $\mu_B$  per Ru atom for polycrystalline  $\text{SrMg}_x\text{Ru}_{1-x}\text{O}_3$  in paramagnetic state



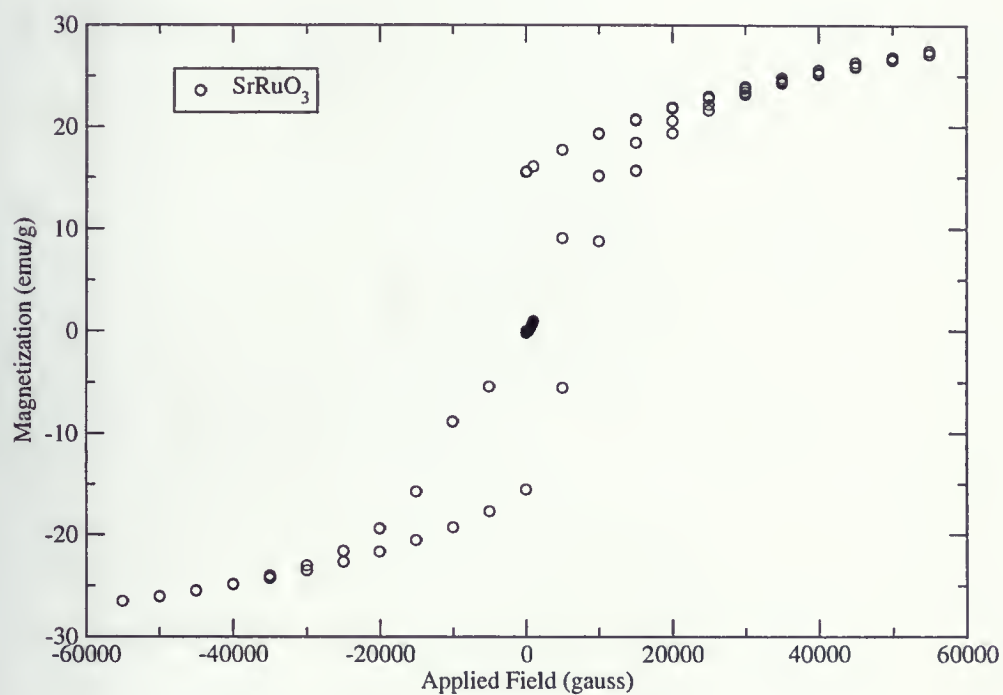


Figure 3.1: Hysteresis Loop for a Polycrystalline Sample of  $\text{SrRuO}_3$  at  $T=5\text{K}$



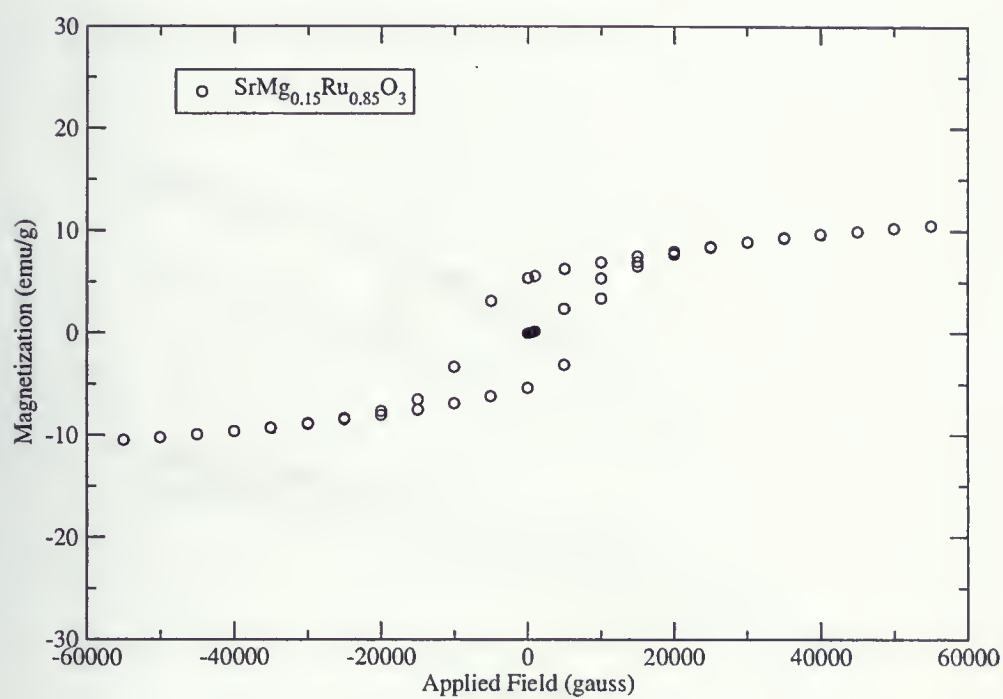


Figure 3.2: Hysteresis Loop for a Polycrystalline Sample of  $\text{SrMg}_{0.15}\text{Ru}_{0.85}\text{O}_3$  at  $T=5\text{K}$



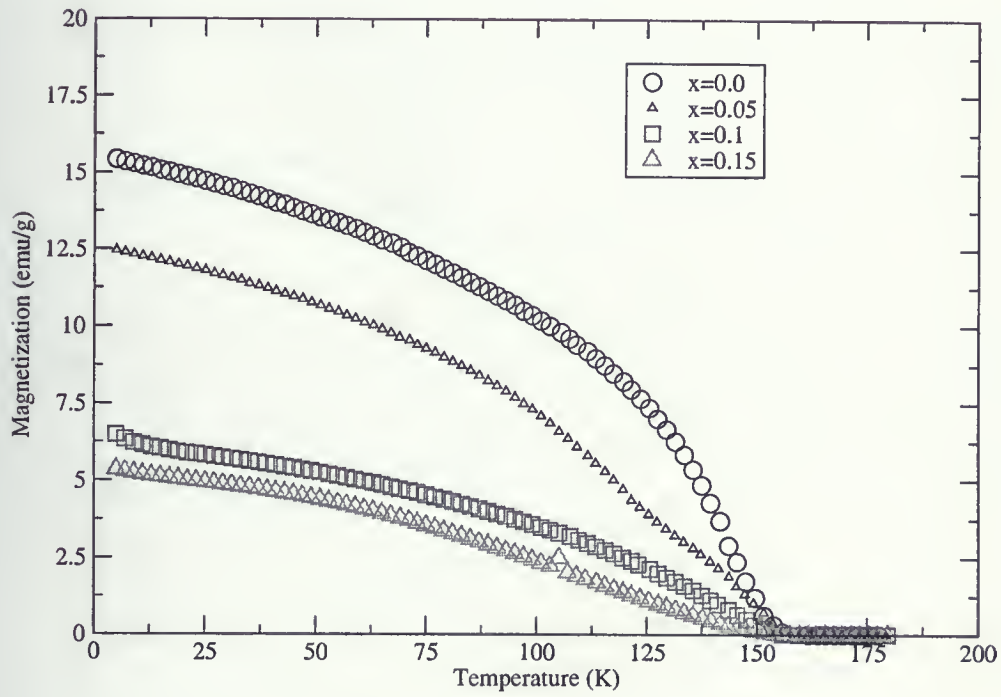


Figure 3.3: Remanent moment vs. temperature for polycrystalline samples



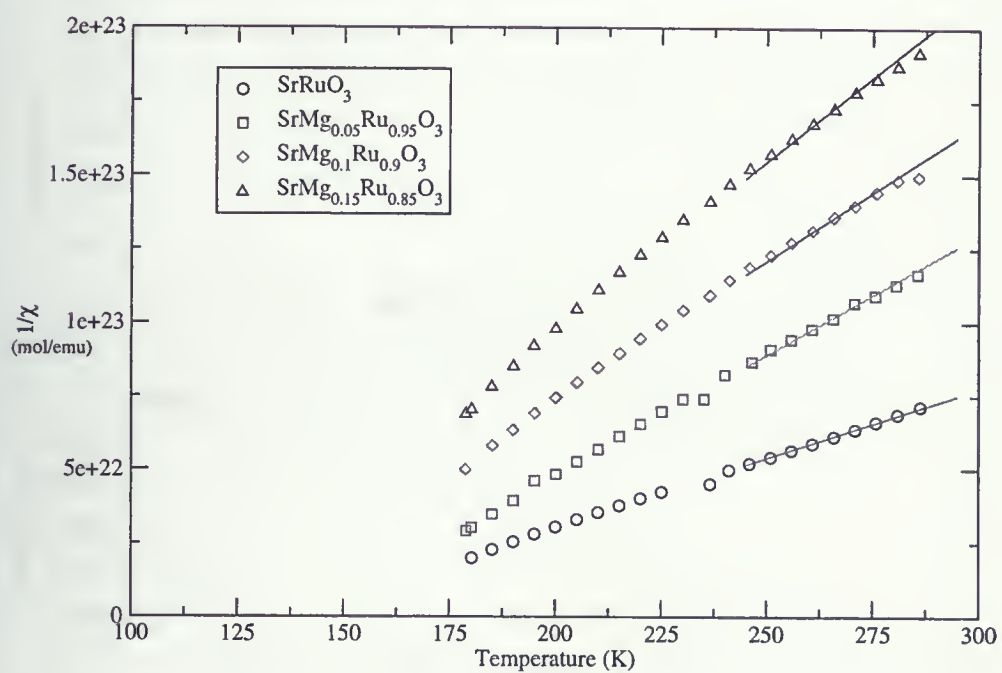
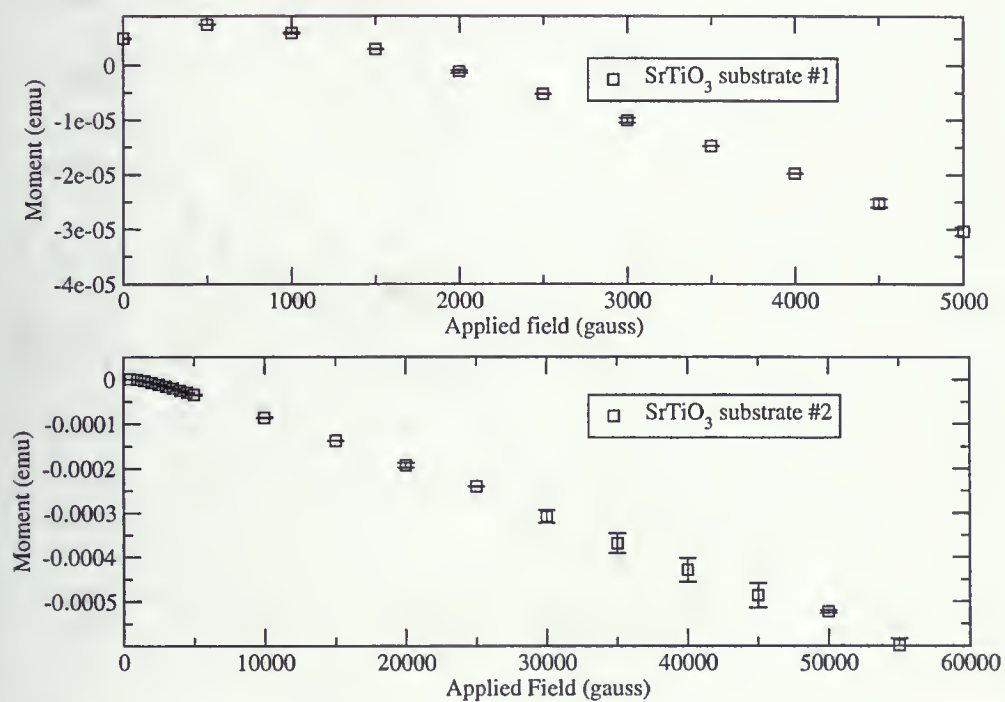


Figure 3.4: Inverse magnetization *vs.* temperature including a linear fit in the range between 245K and 295K



Figure 3.5: Magnetic moment *vs.* Field for substrates at 5K



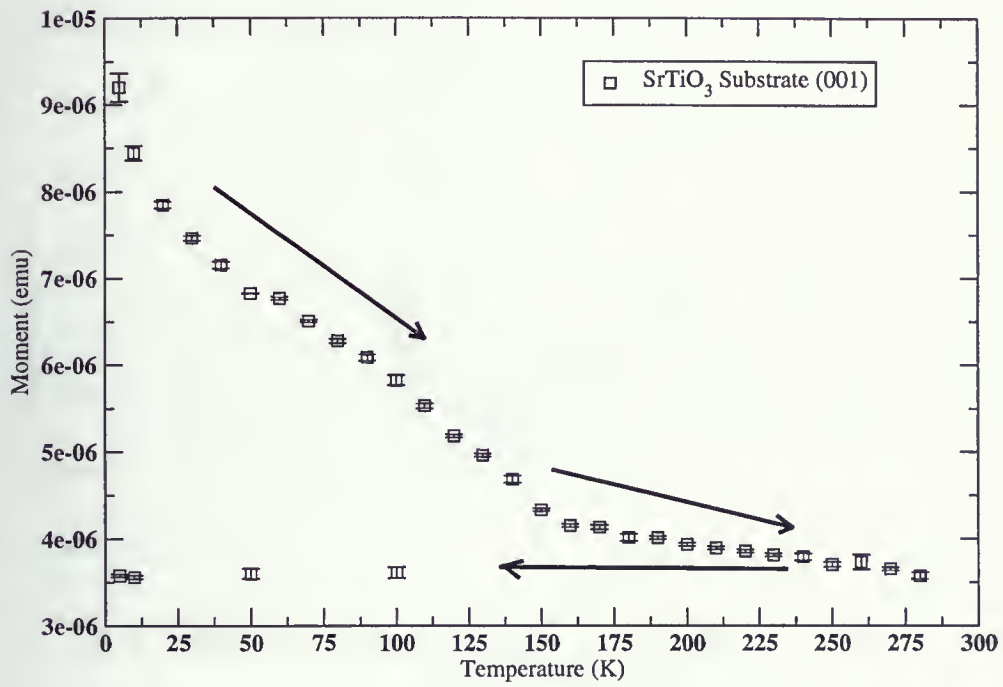


Figure 3.6: Magnetic moment *vs.* temperature at 6 gauss for SrTiO<sub>3</sub> substrate



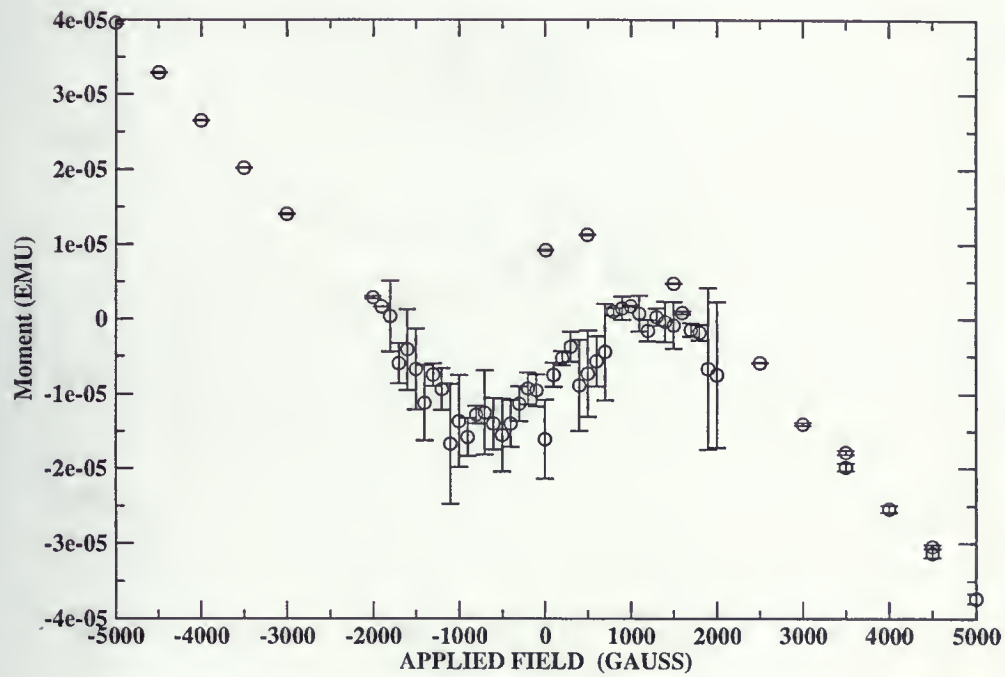


Figure 3.7: Magnetic moment *vs.* field at  $T=5\text{K}$  for  $\text{SrTiO}_3$  substrate



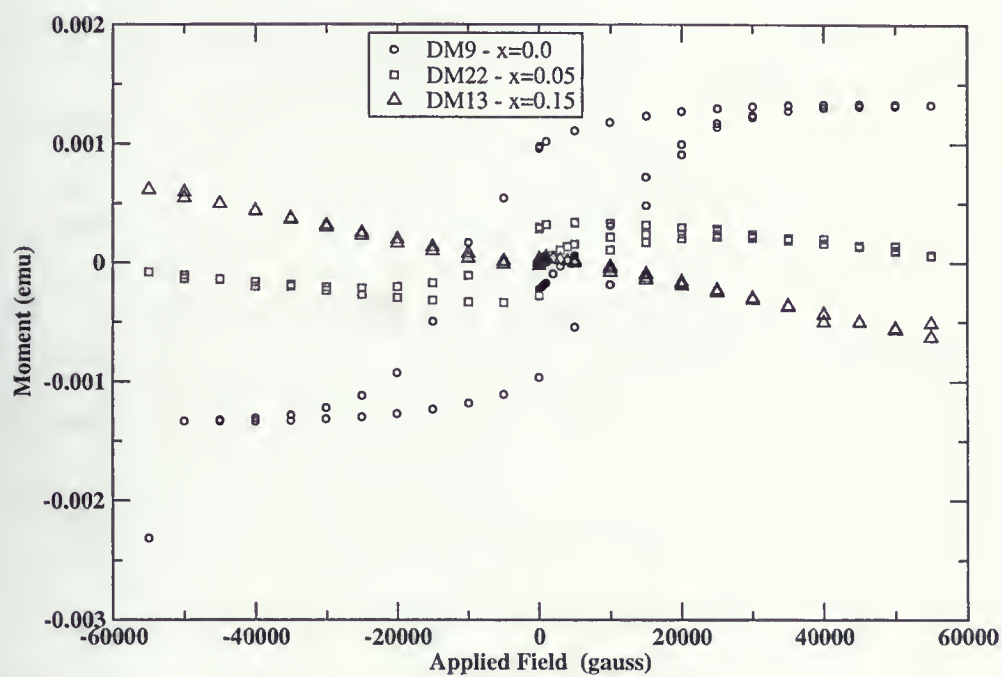


Figure 3.8: Hysteresis curve for thin films grown in  $O_2$  pressure at Substrate Temperature of  $500^\circ C$



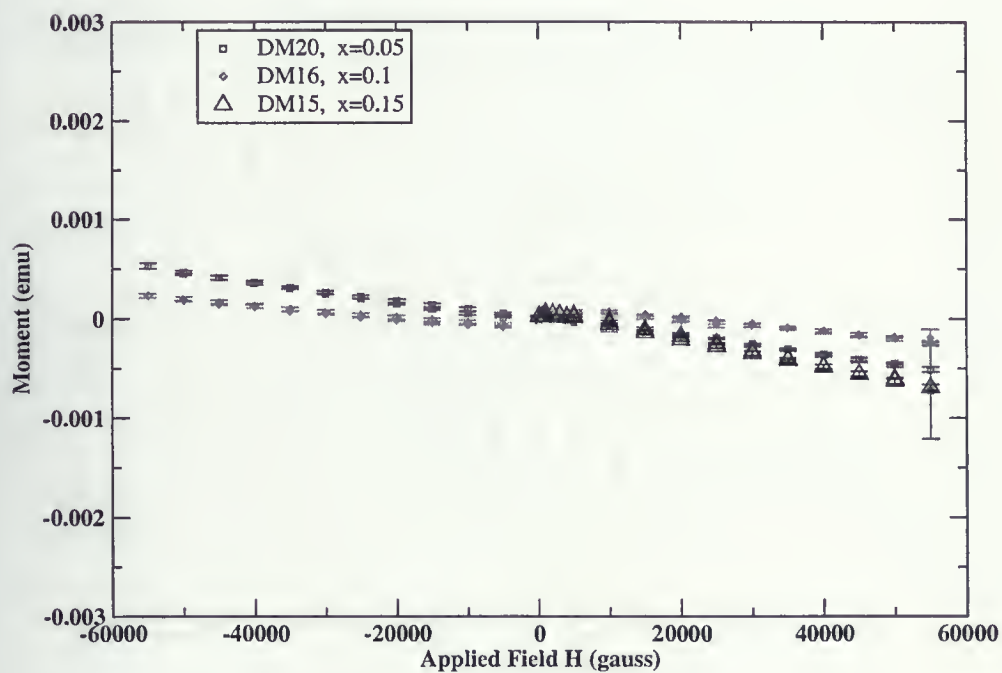


Figure 3.9: Hysteresis curve for thin films grown in Ar pressure at Substrate Temperature of 500°C



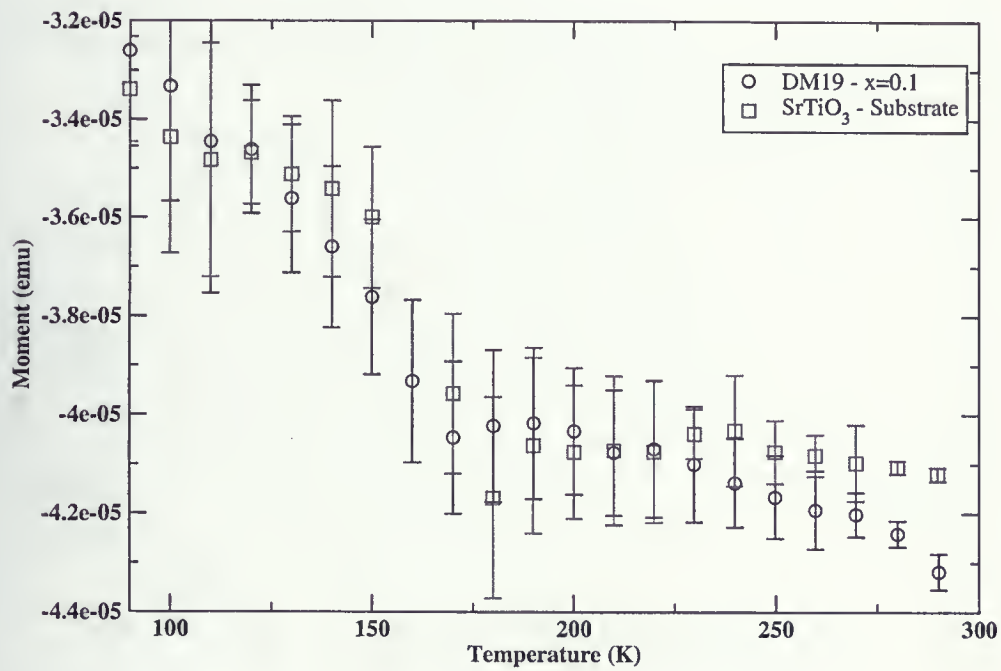


Figure 3.10: Comparing moment *vs.* temperature in 5000G field for Substrate and DM19



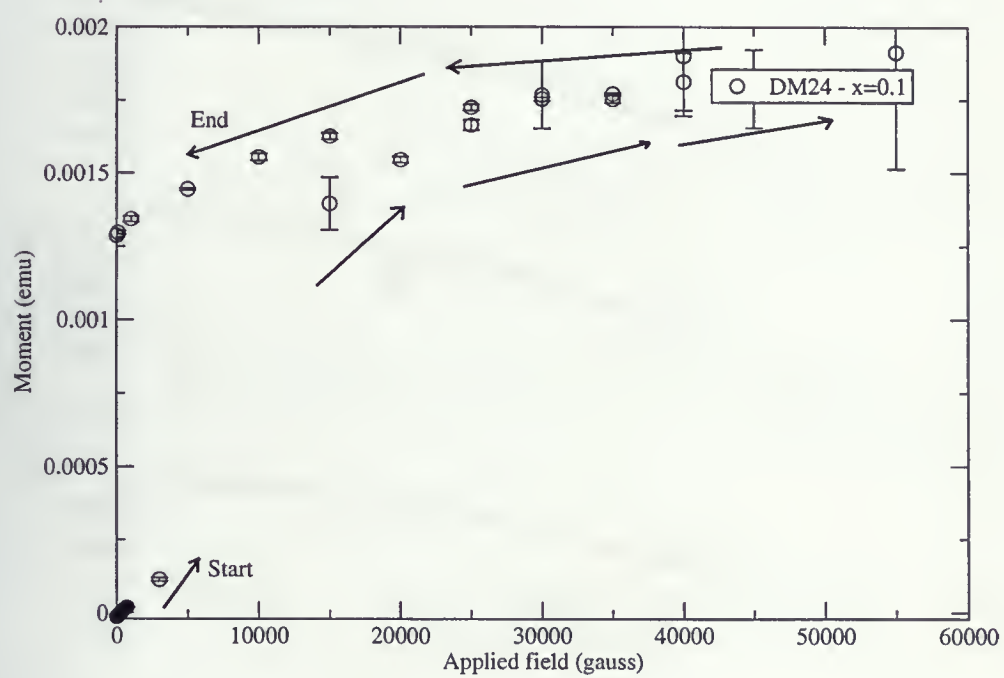


Figure 3.11: Thin film moment *vs.* applied field at 5 K



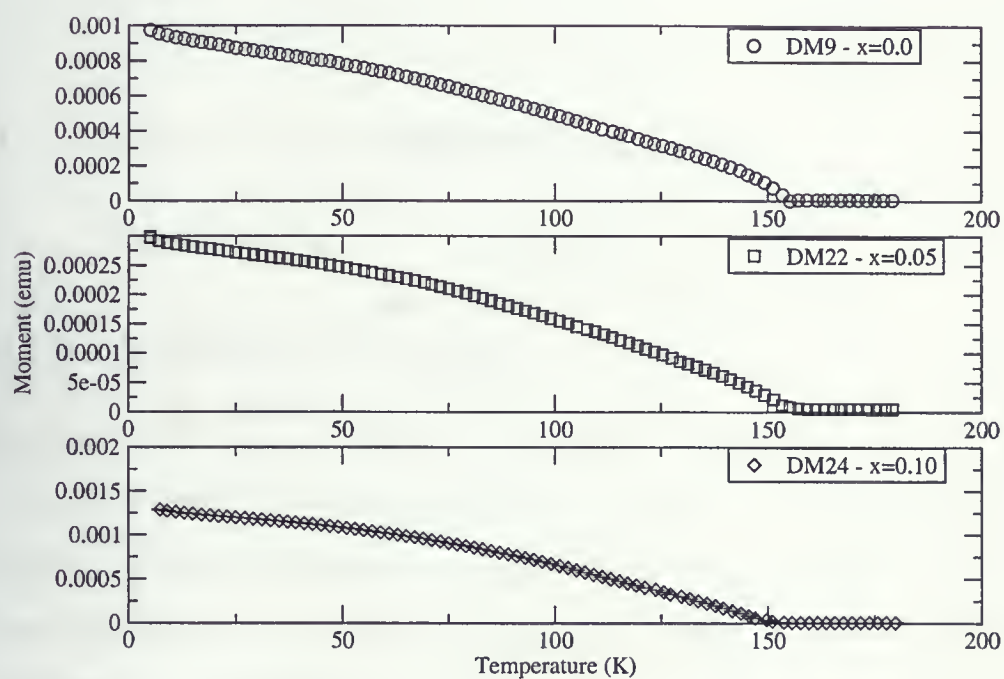


Figure 3.12: Remanent moment *vs.* temperature of DM9, DM22 and DM24 at zero field



# Chapter 4

## Resistivity

### 4.1 Theory of resistivity in metals and insulators

#### 4.1.1 Resistivity in metals

The simplest formula explaining the resistivity of a metal is the Drude equation  $\rho = m^*/ne^2\tau$ , where  $m^*$  is the effective mass of the carriers per unit volume,  $\tau$  is collision time and  $n$  is the number of carriers. Although highly oversimplifying the conduction process [26], it is consistent with more realistic treatments. In simple metals  $n$  is temperature independent, and changes in  $\rho$  are due to the changes in  $\tau$ . According to Matthiessen's rule the resistivity can be decomposed into some physically different models of scattering [15]. The electrical resistivity of most metals is due to collisions of the conduction electrons with lattice phonons, collisions with impurity atoms and/or mechanical imperfections in lattice, the magnetic resistivity due to spin scattering of electrons, and collision between the electrons by themselves. Considering all the mechanisms mentioned above, the total resistivity is cal-



culated by  $\rho_{tot} = \rho_o + \rho_{ph} + \rho_m + \rho_e$ , where  $\rho_o$  is the residual (impurity) resistivity,  $\rho_{ph}$  is the resistivity due to electron-phonon scattering, which appears in the Bloch-Grüneisen equation,  $\rho_m$  is the magnetic resistivity due to spin scattering of electrons [17], and  $\rho_e$  is due to electron-electron interactions. The temperature dependence of the different scattering mechanisms is shown in Fig 4.1. As one see magnetic resistivity (spin-disorder scattering) for  $T > T_c$  is constant. For  $T < T_c$ , there is no general accepted relation between  $\rho_m$  and temperature [20]. Electron-electron collisions yield a term of resistivity proportional to  $T^2$ . There is an argument by Baber<sup>1</sup>, which says that an electron in a state near Fermi Energy  $E_F$  can transfer momentum to another electron only if its energy is within  $\sim k_B T$  of  $E_F$ .

### 4.1.2 Resistivity in insulators

. In a simple filled band insulator the resistivity is determined by  $\rho = \rho_o \exp(E_g/k_B T)$ , where  $E_g$  is energy gap,  $k_B$  is Boltzman constant, and  $n$  number of carriers is proportional to  $\exp(-E_g/k_B T)$ .

There are several models for electron transport in semiconductors and insulators. In intrinsic semiconductors the Conduction Band (CB) is empty and Valence Band (VB) is filled at  $T=0K$  (Fig 4.2), but both CB and VB are delocalized and there is an energy gap  $E_g$  in between them. The carriers can be thermally excited across the energy gap (the process (A) is shown in Fig 4.2). Here the Drude formula is still valid, but the number of carriers  $n$

---

<sup>1</sup>W. G. Baber's argument is noticed in Metal-Insulator transition by Mott [20].



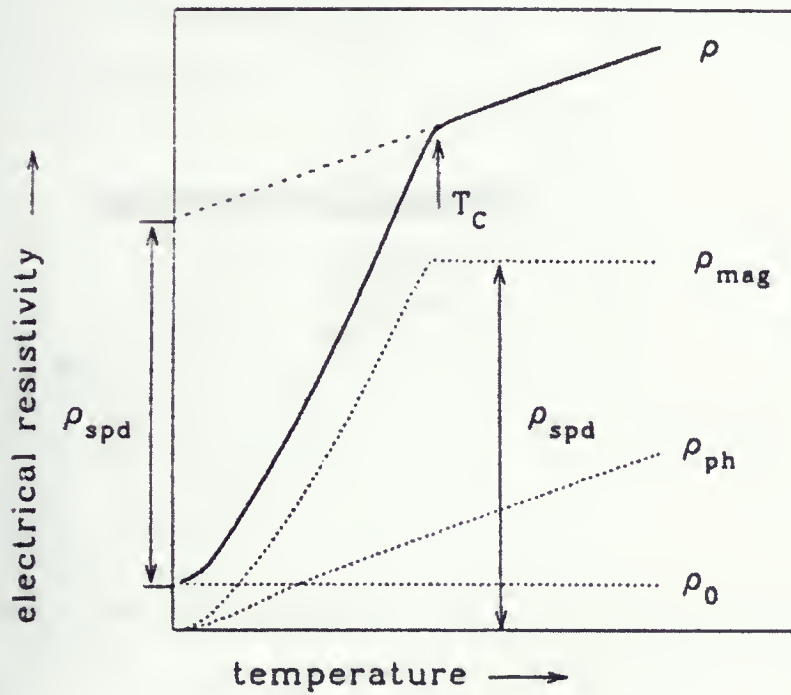


Figure 4.1: A schematic representation of different scattering mechanisms which make up total resistivity [25]



changes with temperature as well as  $\tau$ .

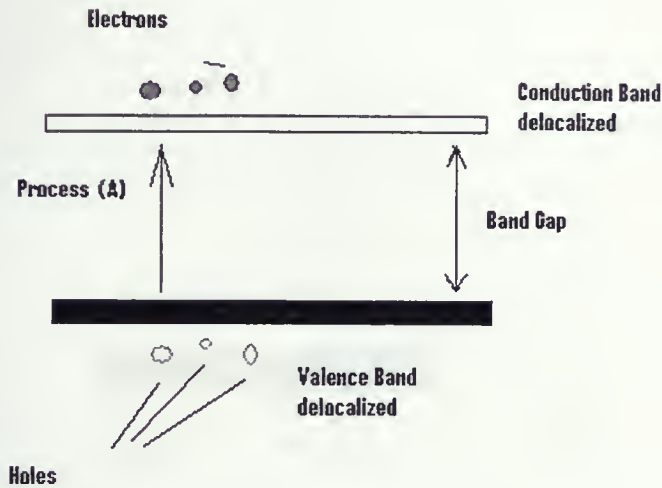


Figure 4.2: Simple band picture for Conduction and Valence band in Semiconductor and Insulators. (A) is excitation of  $e^-$  from VB to CB creating a free  $e^-$  and a free hole in delocalized states.

The effect of impurities is important in insulators. For low impurity concentrations the states of impurities are localized. Excitation from impurity states to conduction band (The process A in Fig 4.3), or hopping from impurity states to impurity states occurs (Variable-Range Hopping)-(the process



B in Fig 4.3). If the impurity density is high enough then an impurity band of delocalized state can be formed . In a localized state, the electron is restricted

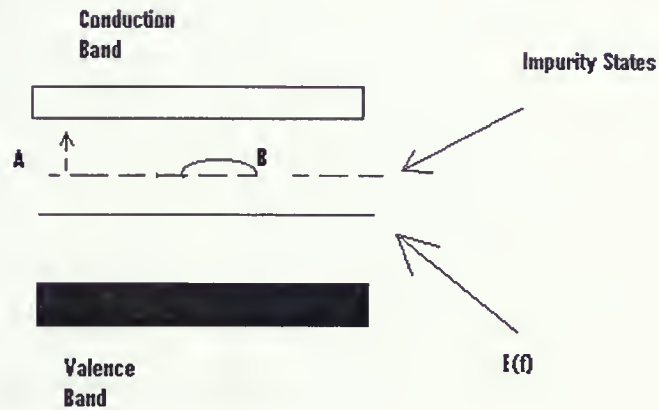


Figure 4.3: Simple band picture for Conduction and Valence band in insulators with impurities, A:excitation of carriers to delocalized states, B:inter-site hopping

to movement around only one particular atomic site, while in a delocalized state the electron is extended throughout the solid [19]. A localized electron is strongly bound to its site, and lies deep within its potential well, separated from the neighbors by high, thick potential barriers. Still a few electrons can



be excited from site to site at room temperature if the barrier is small [19]. This process is known as hopping.

According to the Bloch theorem, in a crystal the band states are delocalized. If there is, for instance, impurities, the main body of the band are delocalized, but the states in a band tail become localized (cross-hatched states of Fig 4.4). The bottom graph of Fig 4.4 shows that mobility is finite in delocalized states but zero in localized states. Since the mobility of a localized electron is zero, so at the tail of the conduction and valence bands the mobility drops fast. Although there is no energy gap, one can see a sharp mobility gap. In a simple words, disorder can cause conduction band to become localized [19].

In the Anderson-transition model the Fermi energy can be in conduction band but disorder can cause CB states to become localized. There might be electron hopping from site to site even in conduction band.

Magnetic insulator is yet another kind of metal-insulator transition and is due to Coulomb repulsion. The Fermi energy level is in conduction band but because of (on-site) electron-electron repulsion  $U$ , there is no conduction, in another word the material become insulator if  $U \geq B$  where  $B$  is bandwidth [19].

### 4.1.3 Variable-range hopping

The electrical resistivity of insulators is governed by variable-range hopping (VRH) at low temperatures [21]. There are two possible conduction mecha-



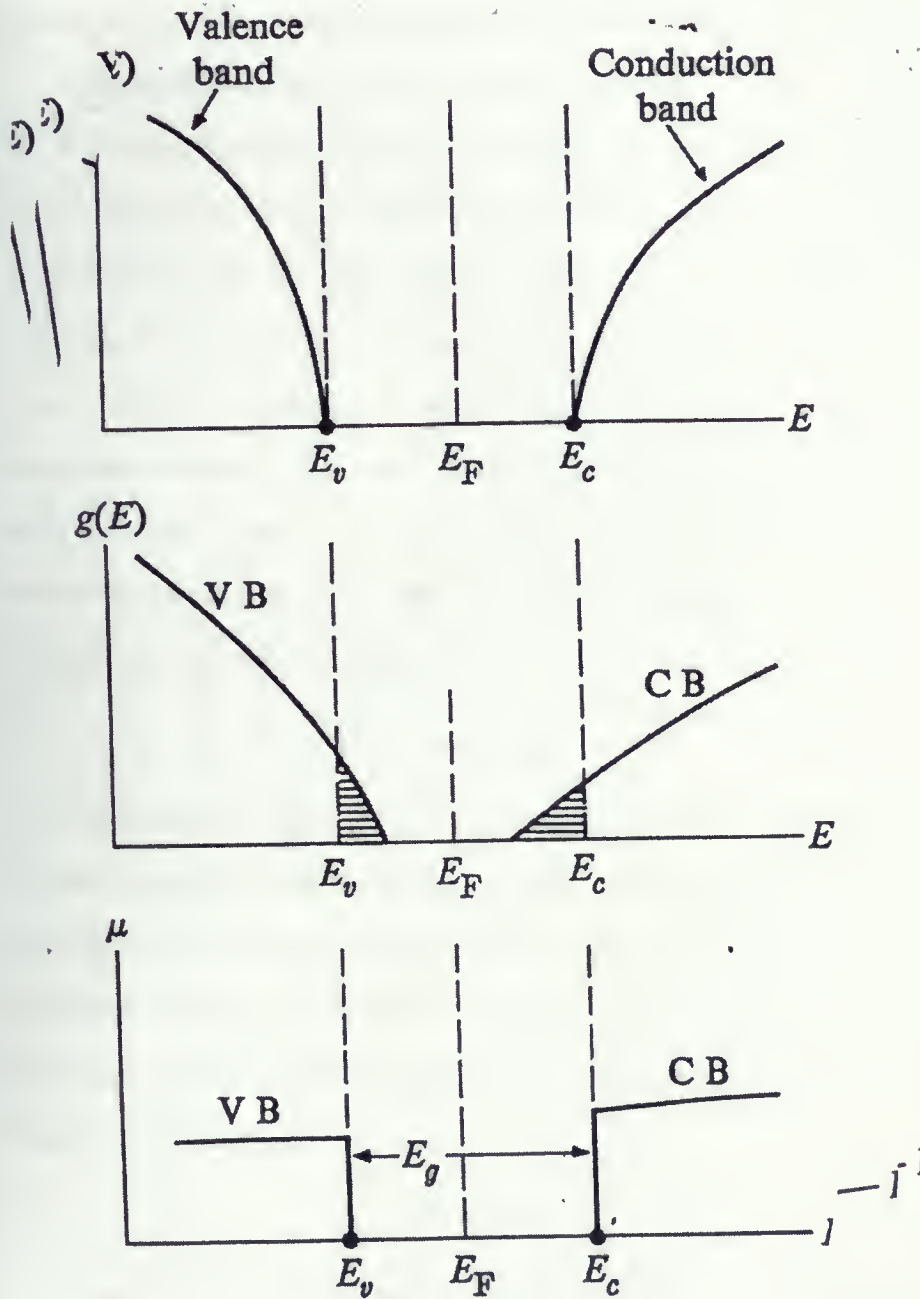


Figure 4.4: Simple band picture for Conduction and Valence band, Anderson Transition [19]



nisms for states in which electrons are localized [20]:

- Excitation of the carrier to a mobility edge.
- If wave functions are localized, so that average of conductivity is zero, then conduction at low temperatures is by thermally activated hopping.

The following definition has been given for VRH by Mott [20]: Every time an electron moves, it hops from one localized state to another, whose wave function overlaps that of the first state. Since the two states have quantized energies, the electron must exchange energy with a phonon(or spin wave)each time it moves. If there is no interaction between electrons, resistivity is obtained from Mott formula [20] which is, where  $\rho_o$  and  $E_o$  are material-dependent constants [10].

$$\rho = \rho_o \exp(E_o/k_B T)^{1/4},$$

It is now realized that it is only near the transition that above equation is valid-and even that is not certain [20]. Another equation in this range developed by Efros and Shklovskii [36]. It basically says if there is a Coulomb repulsion between carriers, it can cause hopping. Then, they introduced following equation where  $E_o = k_B T_o = 2.8e^2/(\kappa a)$  ,  $\kappa$ :dielectric constant,  $a$ : intersite distance.

$$\rho = \rho_o \exp(E_o/k_B T)^{1/2} ,$$

And finally if carriers excited from localized states to delocalized states across a mobility gap. The following equation applies for this model:

$$\rho = \rho_o \exp(E_o/k_B T)$$



## 4.2 Preparing Thin Films for Measurement

There is a method of resistivity measurement developed by L.J.van der Pauw for the samples of arbitrary shape. If the contacts are sufficiently small and located at the circumference of the sample, the specific resistivity can be measured [16].

Four small gold contacts were evaporated near the edge of the samples (Fig 4.5). These thin layers of gold were made in order to have a good possible contact to the system. The contacts are nearly at the circumference of the thin films.

Silver paint glue or soldered Indium was used to make contacts between gold wires and gold contacts on the  $\text{SrRuO}_3$  and  $\text{SrMg}_x\text{Ru}_{1-x}\text{O}_3$  thin films respectively. The thickness of thin films was unknown, so what we measured is resistance [actually it is  $\rho/t$ , resistivity/thickness] versus temperature. All the measurement were begun at room temperature and the temperature then decreased down to 12K. Then again we measured resistance versus temperature while we increased temperature from 12K to 300K. A Continuous Flow Helium Cryostat, manufactured by Helix Technology Corporation, was used for cooling down the samples.



Thin film: four gold wires connected to four gold contacts on the surface of thin film near to circumference, and solder to 4 contacts for van der Pauw measurement (A, B, C, and D)

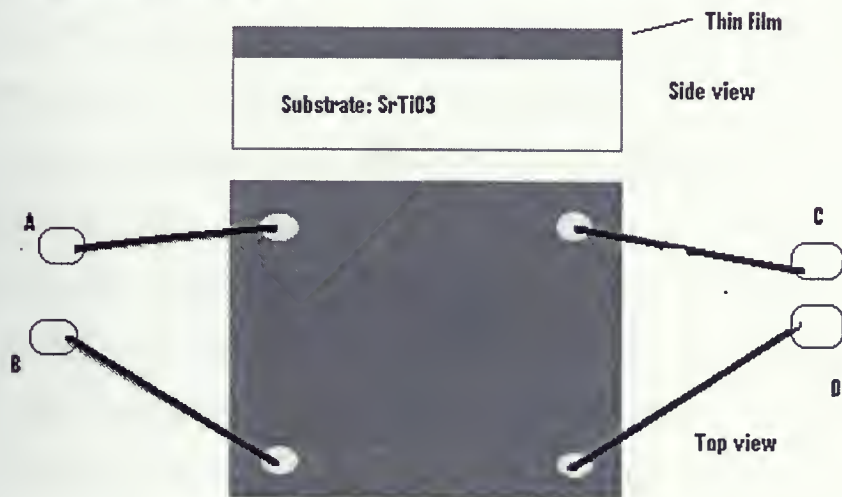


Figure 4.5: Thin film contacts



## 4.3 Results and Graphs

### 4.3.1 Resistivity of SrRuO<sub>3</sub> thin films

In general all of the pure SrRuO<sub>3</sub> thin films that were made exhibited the following general resistivity behaviour (Fig 4.6 and Fig 4.7): The resistivity increased with temperature and the derivative,  $d\rho/dT$ , changed value at the Curie temperature. It was larger for  $T < T_c$  than for  $T > T_c$ . The change in  $d\rho/dT$  is caused by the transition from paramagnetic to ferromagnetic order and the reduction in spin-disorder scattering discussed earlier. These results are consistent with previous works, in which thin films of SrRuO<sub>3</sub> were grown on miscut SrTiO<sub>3</sub> substrates [17], regular SrTiO<sub>3</sub> substrates [17, 8], LaAlO<sub>3</sub> substrates [17], and MgO substrates [4]. We made two tests on pure SrRuO<sub>3</sub> films. We studied the effect of deposition temperature, and the effect of the pressure of the O<sub>2</sub> atmosphere. Fig 4.6 shows the effect of increasing substrate temperature while keeping the oxygen pressure constant. The residual resistivity ratio  $\rho(290K)/\rho(15K)$  which usually increases as the level of impurities decreases in the film is larger for the film grown at 600°C. In figure 4.7, the variation among the DM7, DM9, and DM11 has been caused by different O<sub>2</sub> pressure. Apparently, as oxygen pressure in laser ablation chamber increases, the resistance of thin films decreases. We observed a systematic decrease in resistivity in contrast to earlier work [18]. Note that with different pressures we might get different thickness, which could affect the interpretation of this graph. The ratio between the resistivity at 290K



and 15K for DM7, DM9, DM10 and DM11 are 2.16, 1.96, 3.28, and 2.11 respectively. These resistivity ratio suggest that substrate temperature is more important from oxygen pressure in determining film quality. Our films have higher resistivity ratio than films made by other groups [8].

### 4.3.2 Resistivity of $\text{SrMg}_x\text{Ru}_{1-x}\text{O}_3$ thin films

Four trends were studied: The effect of (I) Mg content (II) atmosphere  $\text{O}_2/\text{Ar}$  (III) substrate temperature (IV) film thickness. We observed that as the amount of Mg in  $\text{SrMg}_x\text{Ru}_{1-x}\text{O}_3$  increases, the resistance of thin films increases. In Fig 4.8 and Fig 4.10, thin films which have been made in  $\text{O}_2$ , show an increase in resistance with increasing Mg content. Thin films which have been made in Ar show the same trend but are more insulating (Fig 4.9). Figure 4.11 illustrates resistivity versus temperature for the thickest film DM24. This sample supposed to be the same as DM19 except for the thickness. DM24 is thicker than DM19. Below 50K curve shows insulating behaviour while for  $T > 50\text{K}$  one can observe the metallic behaviour, which is different from the result obtained for DM19 (see Fig 4.8). Fig 4.8, 4.9, and 4.10 are consistent with the basic trend of increasing Mg increases sample resistance, exhibited by polycrystalline samples [6]. We also studied the effect of substrate temperature on the electrical properties of the films. Fig 4.12 shows that increasing the substrate temperature decreases the resistivity of the  $\text{SrMg}_x\text{Ru}_{1-x}\text{O}_3$  films. This trend is similar to the trend for pure  $\text{SrRuO}_3$  films shown in Fig 4.6.



In summary the plots of resistivity as a function of temperature illustrate four points:

- The resistivity increases with Mg content.
- More insulating thin films were made in Ar than in O<sub>2</sub>.
- High substrate temperatures produce lower resistivity films. This trend should be carefully explored in conjunction with XRD measurement.
- The sample thickness affects the resistivity behaviour as seen in a comparison of DM19 (Fig 4.8) and DM24 (Fig 4.11). DM24 is not epitaxial as discussed in chapter 2. DM19 is a poor quality epitaxial film. It suggests that the microstructure of the film is affecting the resistivity behaviour.

### 4.3.3 Low temperature resistivity in insulating samples

In this section, all three models of hopping discussed earlier are applied to the resistivity data at low temperature ( $15K < T < 50K$ ). The original goal of this thesis was to analyze the  $\rho(T)$  behaviour of the thin films in order to understand the MI transition in  $\text{SrMg}_x\text{Ru}_{1-x}\text{O}_3$ . Before doing this it is useful to examine the complete set of the sample characterization data as listed in table 4.3. One thing that has been learned is that we are not even sure whether  $\text{SrMg}_x\text{Ru}_{1-x}\text{O}_3$  has been grown in Ar atmosphere. There is neither XRD evidence, nor magnetic evidence. Hence films grown in Ar will not be analyzed. There is neither XRD evidence nor mag-



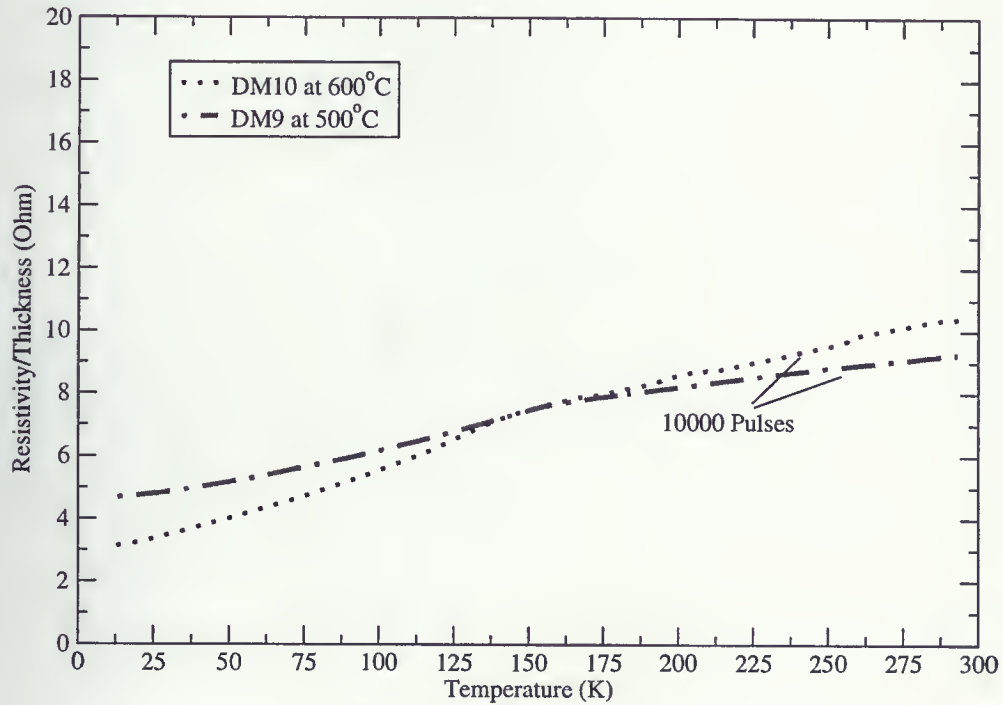


Figure 4.6: Resistivity *vs.* Temperature for Pure  $\text{SrRuO}_3$  Thin Films Grown with Different Substrate Temperatures, but the same  $\text{O}_2$  pressure.



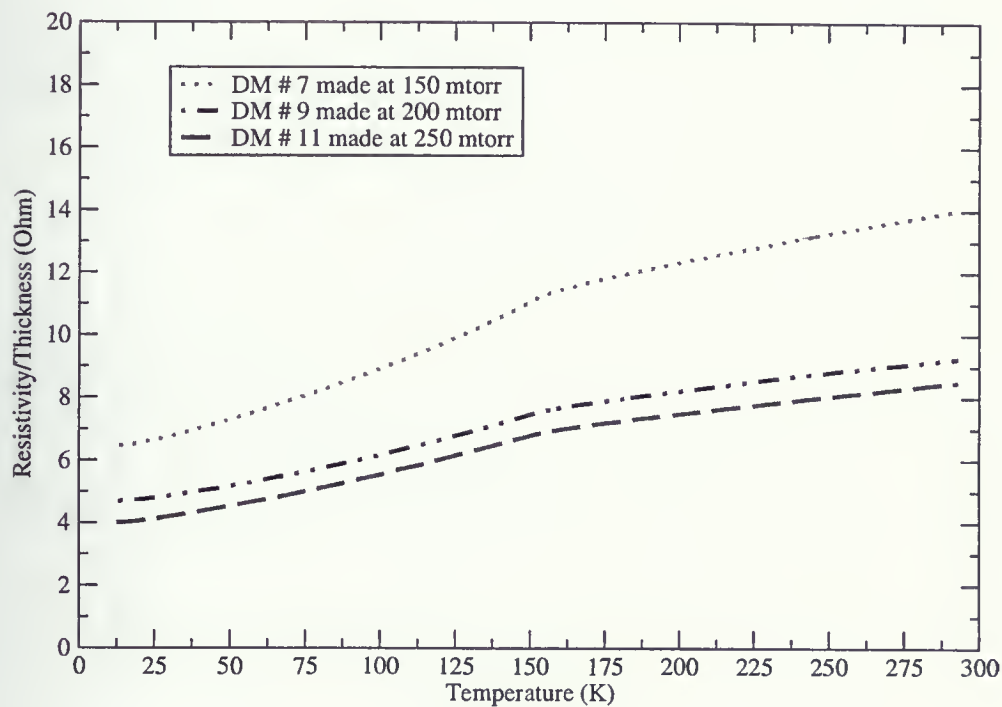


Figure 4.7: Effect of  $O_2$  Pressure, during the Laser Ablation, on Resistivity of  $SrRuO_3$  Thin Films at  $500^\circ C$ . All films were produced by 10000 laser pulses



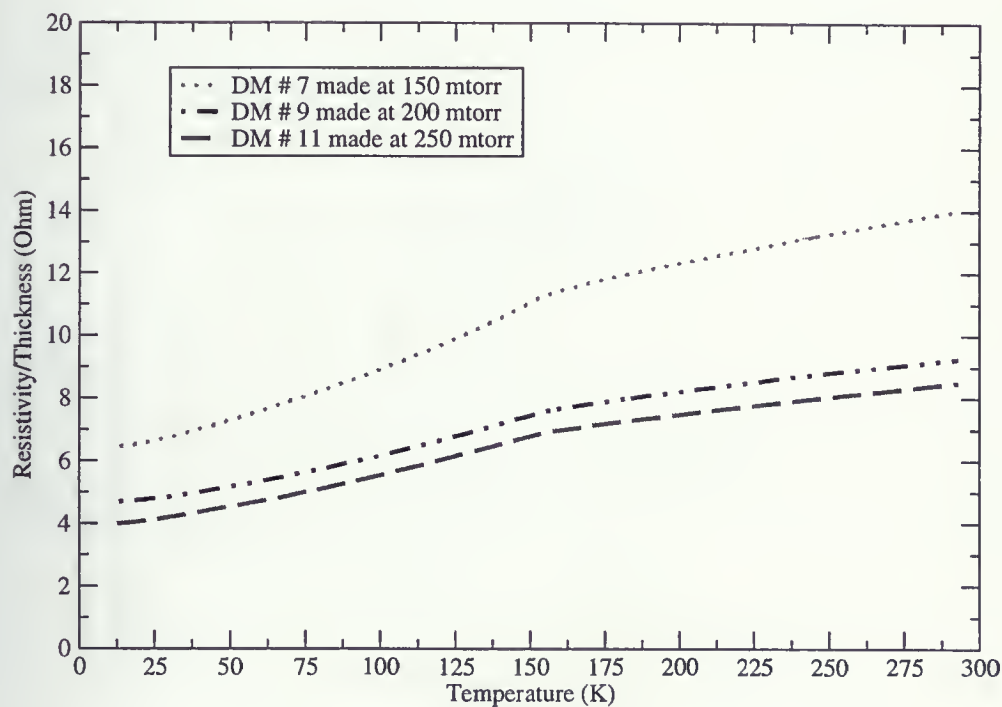


Figure 4.7: Effect of  $O_2$  Pressure, during the Laser Ablation, on Resistivity of  $SrRuO_3$  Thin Films at  $500^\circ C$ . All films were produced by 10000 laser pulses



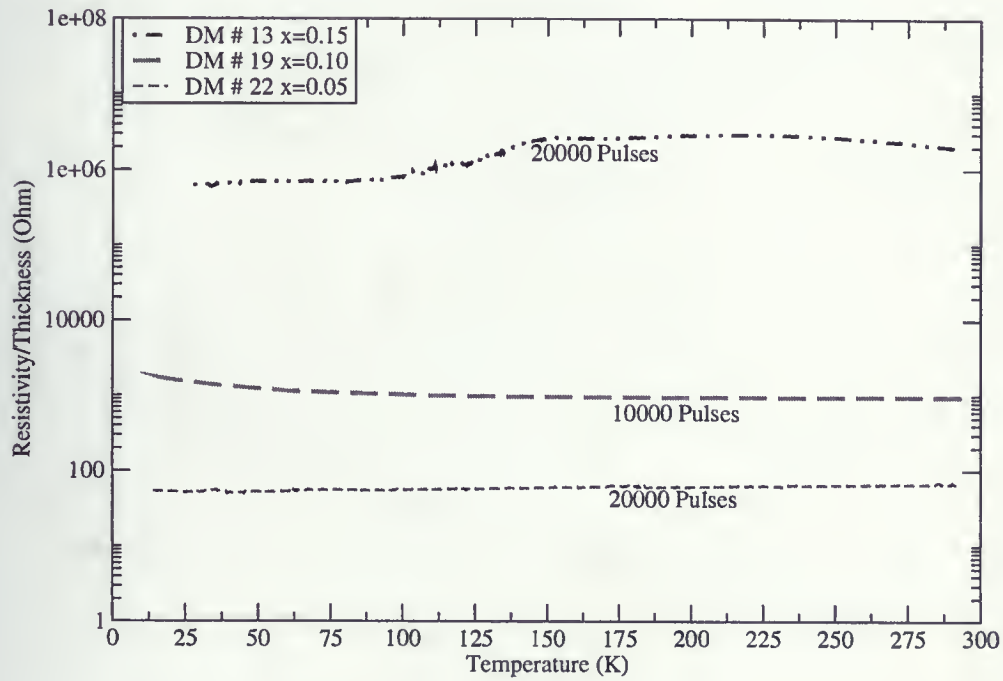


Figure 4.8: Effect of Mg doping on Resistivity in  $\text{SrMg}_x\text{Ru}_{1-x}\text{O}_3$

Thin Films grown in  $\text{O}_2$  at  $500^\circ\text{C}$



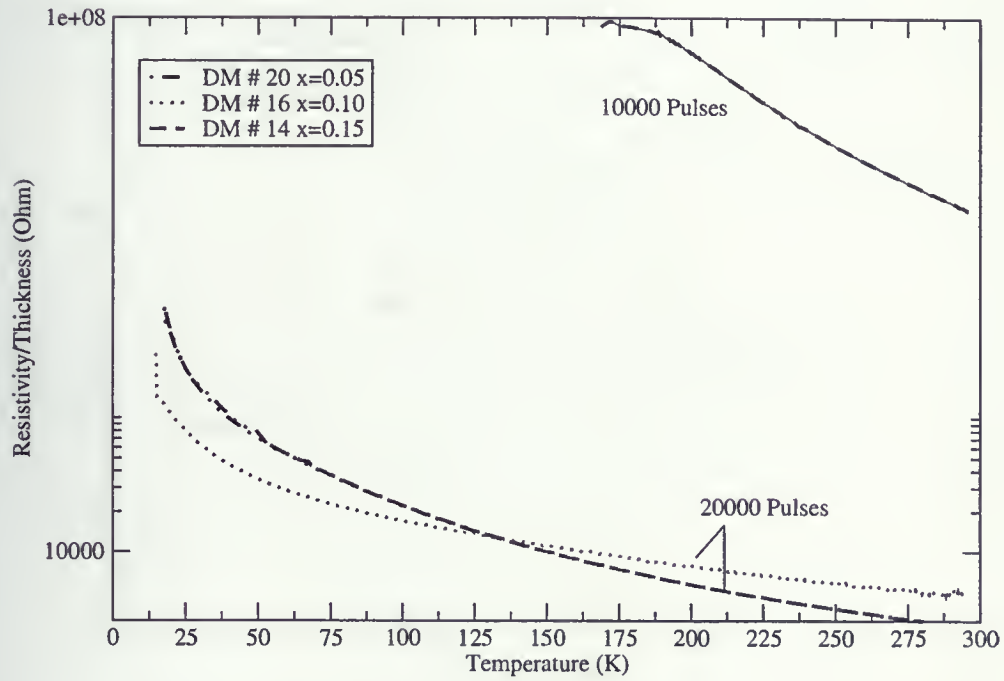


Figure 4.9: Effect of Mg doping on resistivity for  $\text{SrMg}_x\text{Ru}_{1-x}\text{O}_3$

Thin Films Grown in 200 mtorr Ar Pressure, at 500°C



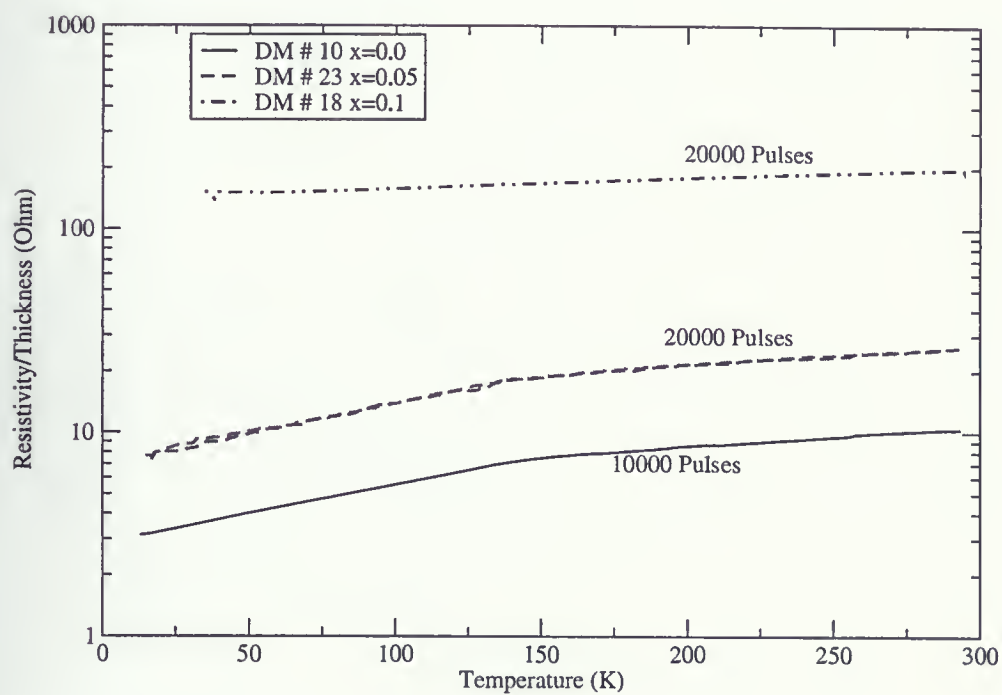


Figure 4.10: Effect of Mg doping on resistivity for SrMg<sub>x</sub>Ru<sub>1-x</sub>O<sub>3</sub>  
Thin Films Grown in O<sub>2</sub> Pressure and 600°C



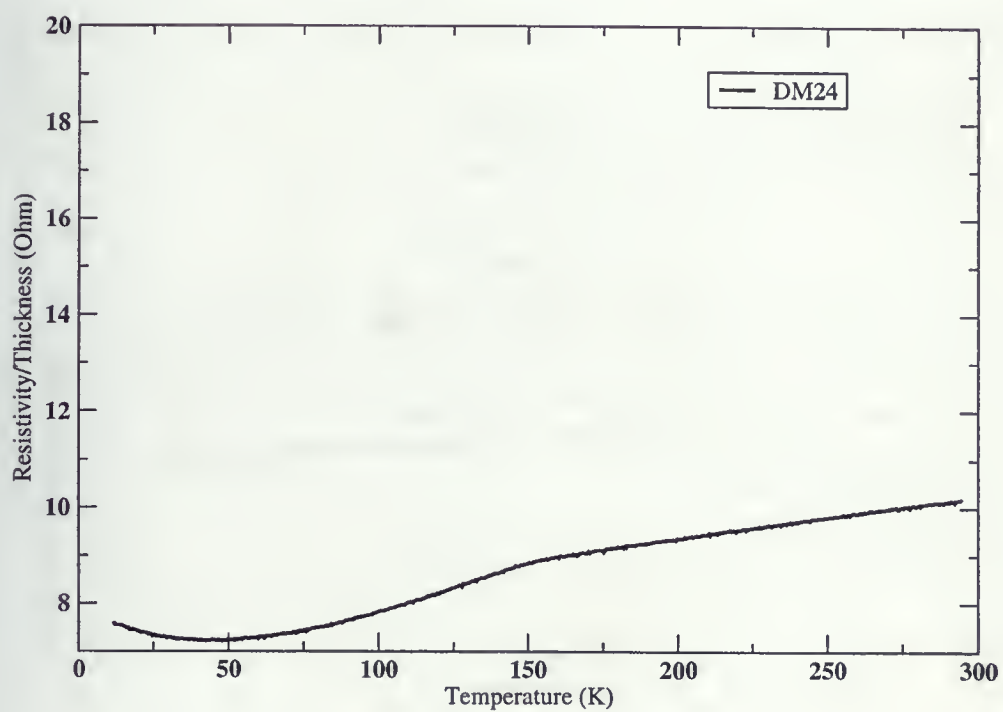


Figure 4.11: Resistance *vs.* Temperature for DM24 Thin Films  
Grown in 200 mtorr O<sub>2</sub> Pressure, at 500°C



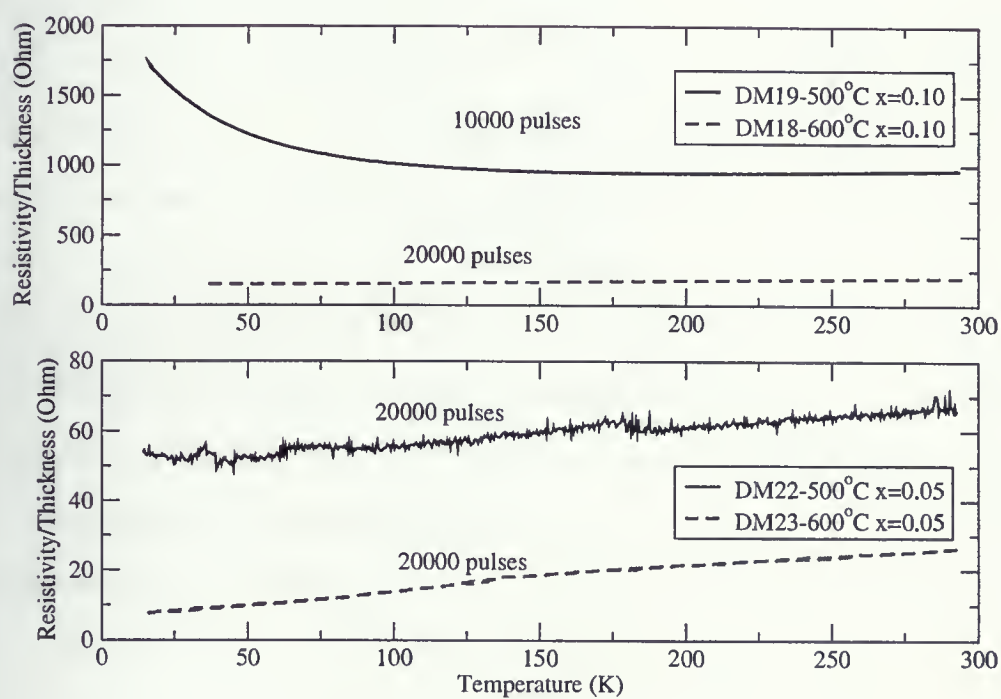


Figure 4.12: Effect of substrate temperature on resistivity of  $\text{SrMg}_x\text{Ru}_{1-x}\text{O}_3$  thin films



netic evidence for successful growth of  $\text{SrMg}_{0.15}\text{Ru}_{0.85}\text{O}_3$ . This leaves the films DM22( $\text{SrMg}_{0.05}\text{Ru}_{0.95}\text{O}_3$ ) and DM19/DM24( $\text{SrMg}_{0.1}\text{Ru}_{0.9}\text{O}_3$ ). DM22 is metallic and hence will not be analyzed. DM19 and DM24 were analyzed for goodness of fit to the various models discussed in section 4.1.3. The equations were linearized (Fig 4.13, Fig 4.14, Fig 4.15), (e.g.  $\ln \rho = \ln \rho_o + (T_o/T)^{1/4}$ ) was plotted as  $\ln \rho$  vs.  $1/T^{1/4}$  and then a goodness of fit parameter  $\Delta = \sum_i (\rho_i - \rho_{theo})^2$  calculated. As can be seen from table 4.2 and 4.3 the best model is simply activated resistivity  $\rho = \rho_o \exp(E_o/k_B T)$ . There is no evidence for variable range hopping in the resistivity data of these samples. The picture presented in Ref.6 that  $\text{Mg}^{2+}$  substituting for  $\text{Ru}^{4+}$  in  $\text{SrMg}_x\text{Ru}_{1-x}\text{O}_3$  causing a metal-insulator transition due to disorder is too simple. Further work must be done to understand the relationship between stoichiometry, sample microstructure, and the electrical and magnetic properties of this material.



Film	gas	target	XRD	EDX (Mg:Ru)	M.b	Res.
DM13	O <sub>2</sub>	x=0.15	NS	NA	NS	Ins
DM15	Ar	x=0.15	NS	NA	NS	Ins
DM16	Ar	x=0.1	NA	NA	NS	Ins
DM18	O <sub>2</sub>	x=0.1	NA	NA	NA	M.h
DM19	O <sub>2</sub>	x=0.1	c=7.85Å	NA	NS	Ins
DM24	O <sub>2</sub>	x=0.1	c=7.87Å	8:92	FM $T_c=155K$	MI
DM20	Ar	x=0.05	NS	NA	NS	Ins
DM22	O <sub>2</sub>	x=0.05	c=7.93Å	NS	FM $T_c=155K$	Ins
DM23	O <sub>2</sub>	x=0.05	NA	NA	NA	M.h
DM25	O <sub>2</sub>	x=0.05	NS	NA	NA	NA

Table 4.1: SrMg<sub>x</sub>Ru<sub>1-x</sub>O<sub>3</sub> Film Characterization Summary, Res.:resistivity M.b:magnetic behaviour, NA:not available, NS:no signal, M:metallic, Ins:insulating, FM:ferromagnetic, M.h:metallic (high  $\rho$ )

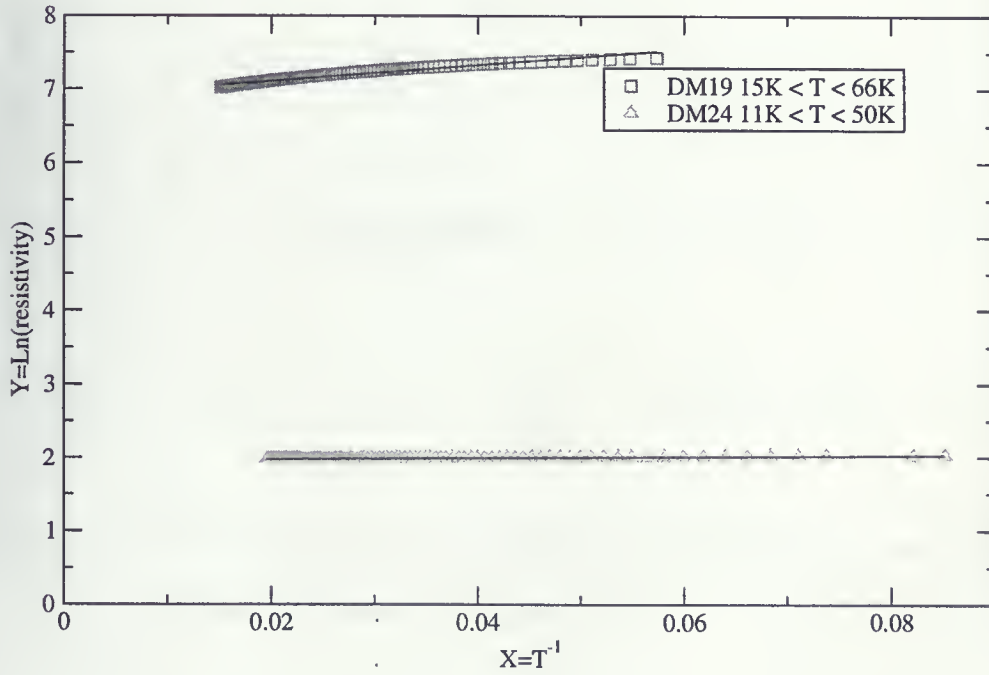
Hopping Model	$T_o$	$\rho_o$	$\Delta$
$\rho = \rho_o \exp(T_o/T)$	$10.9 \pm 0.2$	$984.2 \pm 6$	128593.2
$\rho = \rho_o \exp(T_o/T)^{1/4}$	$12.6 \pm 0.08$	$376.07 \pm 3$	31788834
$\rho = \rho_o \exp(T_o/T)^{1/2}$	$7.7 \pm 0.08$	$709.2 \pm 4$	5475166

Table 4.2: Fitting parameters for different resistivity model-DM19



Hopping Model	$T_o$	$\rho_o$	$\Delta$
$\rho = \rho_o \exp(T_o/T)$	$0.8 \pm 0.02$	$7.08 \pm 0.004$	0.02
$\rho = \rho_o \exp(T_o/T)^{1/4}$	$1.2 \pm 0.02$	$6.4 \pm 0.02$	689.4
$\rho = \rho_o \exp(T_o/T)^{1/2}$	$0.7 \pm 0.01$	$6.8 \pm 0.009$	45.7

Table 4.3: Fitting parameters for different resistivity model-DM24

Figure 4.13: Test for fitting the resistivity of DM19/24 in low temperature range to  $\rho = \rho_o \exp(T_o/T)$



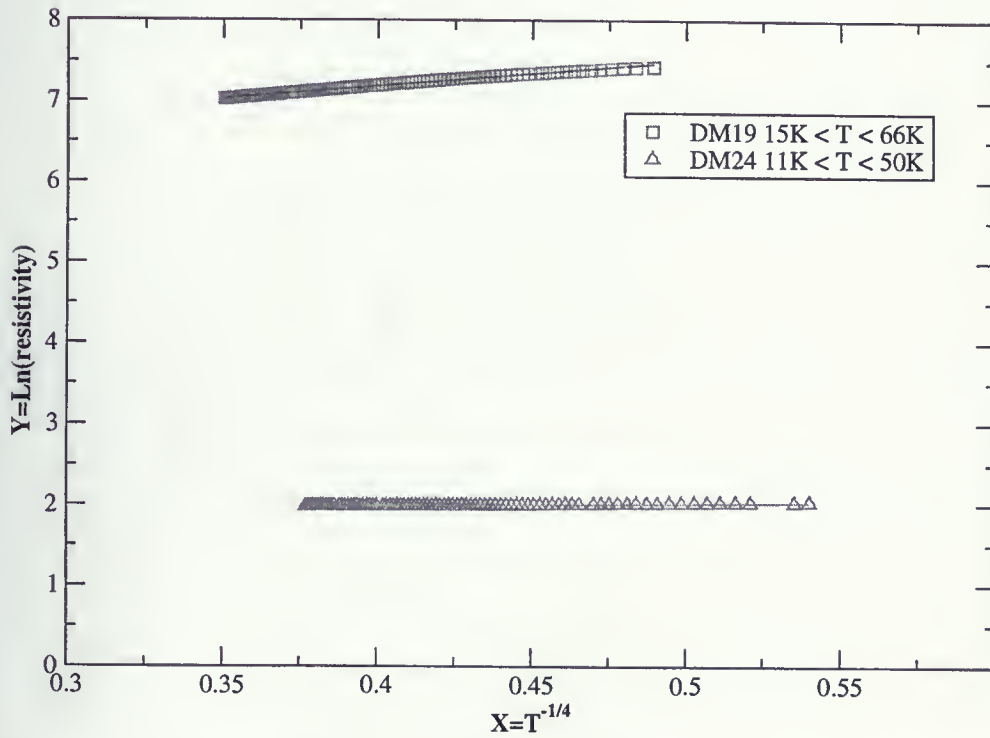


Figure 4.14: Test for fitting the resistivity of DM19/24 in low temperature range to  $\rho = \rho_0 \exp(T_0/T)^{1/4}$



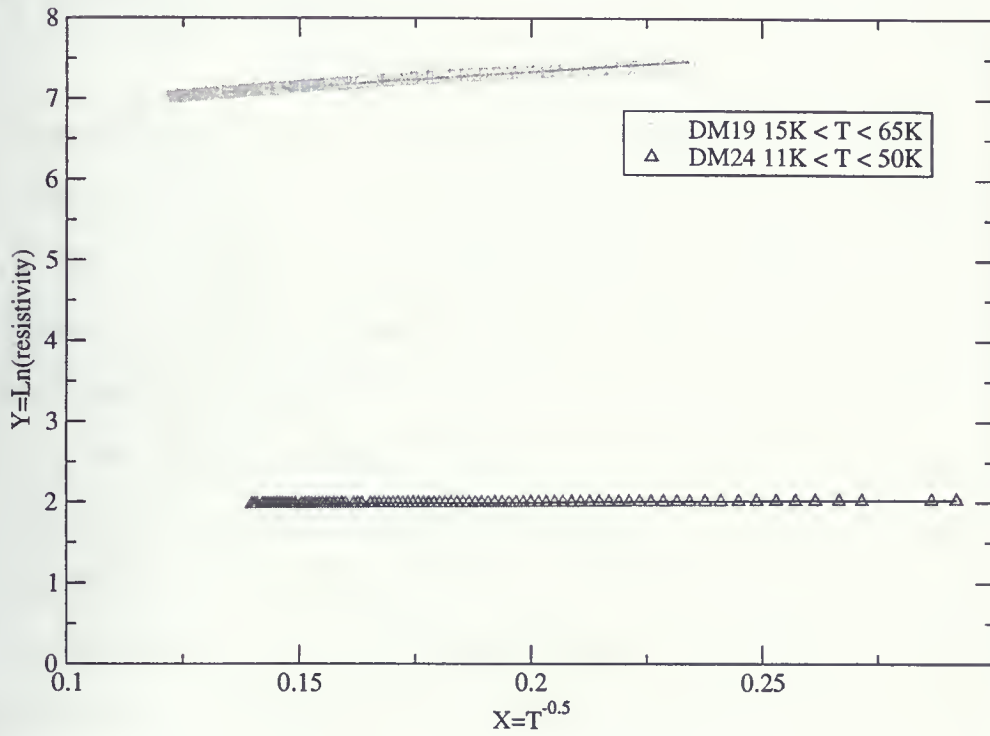


Figure 4.15: Test for fitting the resistivity of DM19/24 in low temperature range to  $\rho = \rho_0 \exp(T_0/T)^{1/2}$



# Chapter 5

## Conclusions

Making epitaxial thin films of  $\text{SrMg}_x\text{Ru}_{1-x}\text{O}_3$  was our first goal of this project. We were successful in growing films for  $x = 0.0$ ,  $x = 0.05$ , and  $x = 0.10$ . In particular, the epitaxial growth of DM22 ( $x = 0.05$ ) was good. We were not successful in growing  $x = 0.15$ . We learned several things that could guide further research:

- Films should be grown in  $\text{O}_2$  not Ar.
- The film resistivity is decreased by increasing substrate temperature from  $500^\circ\text{C}$  to  $600^\circ\text{C}$ . This effect should be further explored in conjunction with XRD, EDX, and electron microscopy to separate the effects of microstructure and sample stoichiometry on the electrical properties of the thin films, the thickness of the film effects, epitaxial quality and resistivity.
- Thin films of  $\text{SrMg}_{0.05}\text{Ru}_{0.95}\text{O}_3$  and  $\text{SrMg}_{0.1}\text{Ru}_{0.9}\text{O}_3$  have similar magnetic behaviour (ferromagnetic,  $T_c \sim 155\text{K}$ ) to polycrystalline samples.
- The Mg content of thin films is comparable to content of polycrystalline target (e.g. EDX study of DM24). This trend should be explored further.

Unfortunately the study of the temperature dependence of resistivity did not lead us to a clear understanding of MI transition in  $\text{SrMg}_x\text{Ru}_{1-x}\text{O}_3$ . The



---

fact that the resistivity of  $x=0.1$  films showed all three kinds of behaviour (metallic, insulating, and metal-insulator transition) points out the need for more work to separate the effects of stoichiometry and microstructure in these materials.



## Bibliography

- [1] D. J. Singh, "Electronic and magnetic properties of the 4d itinerant ferromagnet  $\text{SrRuO}_3$ " J. Appl. Phys. **79**, 4818 (1996)
- [2] L. Mieville, T. H. Geballe, L. Antognazza, and K. Char, "Ti and Ca substitution in  $\text{SrRuO}_3$  thin films by sequential deposition process" J. Appl. Phys. Lett. **70** 126 (1997).
- [3] X. D. Wu, S. R. Foltyn, R. C. Dye, Y. Coulter, and R. E. Muenchausen, "Properties of epitaxial  $\text{SrRuO}_3$  thin films" Appl. Phys. Lett. **62**, 2434 (1993).
- [4] Z. Sefrioui, D. Arias, M. A. Navacerrada, M. Varela, G. Loos, M. Lucia, J. Santamaria, F. Sanchez-Quesada, and M. A. Lopez de la Torre, "Metal-Insulator transition in  $\text{SrRuO}_3$  induced by ion irradiation" Appl. Phys. Lett. **73**, 3375 (1998).
- [5] G. Cao, S. McCall, J. Bolivar, M. Shepard, F. Freibert, P. Henning, and J. E. Crow, "Itinerant-to localized electron transition in  $\text{CaRu}_{1-x}\text{Sn}_x\text{O}_3$  and  $\text{SrRu}_{1-x}\text{Pb}_x\text{O}_3$ " 54 Physical Review B, **54**, 14144 (1996)



- 
- [6] D. A. Crandles, M. Reedyk, R. W. Schaeffer, A. E. Hultgren, and R. Schlee, "Metal-insulator transition in the  $\text{SrRu}_{1-x}\text{Mg}_x\text{O}_3$  system", *Physical Review B*, **65**, 224407, (2002).
- [7] Web Site: <http://www.crystallmaker.co.uk>.
- [8] C. L. Chen, Y. Cao, Z. J. Huang, Q. D. Jiang, Z. Zhang, Y. Y. Sun, W. N. Kang, L. M. Dezaneti, W. K. Chu, and C. W. Chu, "Epitaxial  $\text{SrRuO}_3$  thin films on (001)  $\text{SrTiO}_3$ " *Appl. Phys. Lett.* **71** 1047 (1997).
- [9] R. Kelly, A. Miotello, D. B. Chrisey, J. Wilery, "Mechanisms of pulsed laser sputtering in pulsed laser deposition of thin film" New york, (1994)
- [10] D. S. Zemmerman, and M. R. A. Shegelski, "Three-dimensional numerical simulation for activated hopping conduction" *Phys. Rev. B*, **38**, 3, (1998).
- [11] Web Site: <http://www.hut.fi/Units/AES/projects/prlaser/thesis/node4.html>.
- [12] P. Rhodes and E. P. Wohlfarth, "The effective Curie-Weiss constant of ferromagnetic metals and alloys" *Proc. R. Soc London*, **273**, 247, (1962).
- [13] G. Cao, L. Balicas, W. H. Song, Y. P. Sun, Y. Xin, V. A. Bondarenko, J. W. Brill, S. Parkin, X. N. Lin, "Competing ground states in triple-layered  $\text{Sr}_4\text{Ru}_3\text{O}_{10}$ : Verging on itinerant ferromagnetism with critical fluctuation" *Phys. Rev. B*. **68**, 174409 (2003).



- 
- [14] C. W. Jones, P. D. Battle, P. Lightfoot, and W. T. A. Harrison, "The structure of  $\text{SrRuO}_3$  by time of flight neutron powder diffraction" *Acta Cryst. C* **45**, 365, (1989).
- [15] C. Kittel, *Introduction to Solid State Physics*, Seventh Edition, (New York: John Wiley and Sons, Inc., 1996).
- [16] L. J. van der Pauw, "A method of measuring specific resistivity and hall effect of discs of arbitrary shape" *Philips Res. Repts.* **13** (1958).
- [17] L. Klein, J. S. Dodge, J. W. Reiner, L. Mieville and T. H. Geballe, M. R. Beasley and A. Kapitulnik, "Transport and magnetization in the badly metallic itinerant ferromagnet  $\text{SrRuO}_3$ ", *J. Phys.:Condens. Matter.* **8**, 10111 (1996).
- [18] X. Fang, T. Kobayashi, "Characterization of  $\text{SrRuO}_3$  thin film grown by laser ablation at temperature above  $400^\circ\text{C}$ " *Journal of Applied Physics*, **90**, 162 (2001).
- [19] M. A. Omar, *Elementary solid state physics*, (London: Addison-Wesley Publishing Company, 1975).
- [20] N. Mott, *Metal-insulator transitions*, (London: Taylor and Francis, 1990).
- [21] Y. Zhang, P. Dai, M. Levy, and M. P. Sarachik, "Probing the Coulomb Gap in Insulating n-type  $\text{CdSe}$ " **64**, 2687, (1990)



- 
- [22] L. Antognazza, K. Char, T. H. Geballe, L. L. H. King, and A. W. Sleight, "Josephson coupling of  $\text{YBa}_2\text{Cu}_3\text{O}_{7-x}$  through a ferromagnetic barrier  $\text{SrRuO}_3$ " *Appl. Phys. Lett.* **63**, 7, (1993).
- [23] R. J. Bouchard, J. L. Gillson, "Electrical properties of  $\text{CaRuO}_3$  and  $\text{SrRuO}_3$  single crystals" *Mater. Res. Bull.* **7**, 873 (1972).
- [24] A. Callaghan, C. W. Moeller, and R. Ward, "Magnetic interactions in ternary ruthenium oxides" *Inorg. Chem.* **5**, 1572, (1966).
- [25] J. M. Fournier, and E. Gratz, "Transport properties of rare earth and actinide intermetallics" *Handbook on the physics and chemistry of rare earths*, Elsevier science publishers B. V. **17**, 409 (1993)
- [26] N. W. Ashcroft, N. D. Mermin, *Solid State Physics*, (Philadelphia: Saunders College, 1976).
- [27] P. B. Allen, H. Berger, O. Chauvet, L. Forro, T. Jarlborg, A. Junod, B. Revaz, and G. Santi, "Transport properties, thermodynamic properties, and electronic structure of  $\text{SrRuO}_3$ " *Phys. Rev. B*, **53**, 4393, (1996).
- [28] Y. Noro and S. Miyahara, "Electrical resistivity of  $\text{SrRuO}_3$ " *J. Phys. Soc. Jpn*, **27**, 518, (1969).
- [29] M. Shikano, T. K. Huang, Y. Inaguma, M. Itoh, and T. Nakamura, "Pressure dependence of the magnetic transition temperature for ferromagnetic  $\text{SrRuO}_3$ " *Solid State Commun*, **90**, 115, (1983).



- 
- [30] H. P. R. Frederikse and George A. Candela, "Magnetic Susceptibility of Insulating and Semiconducting Strontium Titanate" *Physical Review* **147** 2, 583 (1966)
- [31] T. Kiyama, K. Yoshimura, K. Kosuge, H. Mitamura and T. Goto, "High-Field magnetization of  $\text{Sr}_{1-x}\text{Ca}_x\text{RuO}_3$ " *J. of the Physical Society of Japan*, **68**, 10 (1999).
- [32] Manufactured by CrysTec-KRISTALLTECHNOLOGIE, Size:  $5\text{mm} * 5\text{mm} * 1\text{mm}$
- [33] F. Razavi, Private communication.
- [34] S. Yaghoubzadeh, *MSc Thesis*, (1999)
- [35] Web Site: <http://www.asu.edu/clas/csss/chrem/techniques/EDX.html>.
- [36] A. L. Efros, B. L. Shklovskii, "Percolation theory and conductivity of disordered systems" *Journal of Physics*, **C8**, L49, (1975)
- [37] A. Brodyanski, S. Medvedev, M. Minenko, H. J. Jodl, "Solid oxygen as low dimensional system by spectroscopic studies" *Application of High Pressure to Low-Dimensional Novel Electronic Materials*, Netherlands, H. D. Hochheimer *et al.*, Kluwer (2001)









